

REDUCED MEMBRANE MODEL FOR LIQUID CRYSTAL POLYMER NETWORKS: ASYMPTOTICS AND COMPUTATION

LUCAS BOUCK, RICARDO H. NOCHETTO, AND SHUO YANG

ABSTRACT. We examine a reduced membrane model of liquid crystal polymer networks (LCNs) via asymptotics and computation. This model requires solving a minimization problem for a non-convex stretching energy. We show a formal asymptotic derivation of the $2D$ membrane model from $3D$ rubber elasticity. We construct approximate solutions with point defects. We design a finite element method with regularization, and propose a nonlinear gradient flow with Newton inner iteration to solve the non-convex discrete minimization problem. We present numerical simulations of practical interests to illustrate the ability of the model and our method to capture rich physical phenomena.

1. INTRODUCTION

Liquid crystal polymer networks (LCNs) are materials that combine elastomeric polymer networks with mesogens (compounds that display liquid crystal properties). The long rod-like molecules of liquid crystals are *densely* crosslinked with the elastomeric polymer network. This contrasts with liquid crystal elastomers (LCEs), whose crosslinks are less dense. The orientation of the liquid crystal (LC) molecules can be represented by a director. The orientation of the director influences deformation of materials when actuated. Common modes of actuation are heating [1, 2] and light [3, 4].

LCNs are one of many possible materials that enable spontaneous mechanical motion under a stimulus. This has been referred to as “the material is the machine” [5]. Due to this feature, engineers create soft robots using LCNs/LCEs materials, such as thermo-responsive micro-robots with autonomous locomotion in unstructured environments [6], soft materials that “swim” away from light [3], and LCN actuators that can lift an object tens of times its weight [2]. They offer abundant application prospects, for instance in the design of biomedical devices [7, 8].

Since the deformation of LCNs depend on the orientation of the nematic director, the director can be blueprinted or programmed so that the materials achieve desired shapes [1, 9, 10, 11]. Some methods to program the orientation of the liquid crystals include mechanical alignment [3], photoalignment [2], and additive manufacturing [12], which is a subset of 4D printing [13]. Even if the director is constant throughout the material, interesting shapes may occur due to nonuniform actuation. An example of nonuniform actuation from light is the LCE swimmer in [3]. Two reviews of experimental work on LCEs/LCNs can be found in [9, 14].

For 3D bodies, one of the most accepted elastic energies for modeling the interaction of the material deformation with the LCs is known as the *trace formula* [15, 16, 17], although other types of elastic energies have been proposed [18].

Date: October 7, 2022.

Depending on the density of crosslinks, the director field may be either totally free [19, 20] or subject to a Frank elasticity term [21, 22, 23, 24]. This kind of blueprinted configuration describes the situation where the LCs are unconstrained or constrained only on a low-level by rubbery polymers. On the other hand, the LCs may also be frozen into the material via direct algebraic constraint [25, 26] or a physically justified penalization [23, 27]. Although the LCs may be described by the Frank energy, a key modeling difference between LCE/LCNs and nematic LCs is that the former are constrained by the rubber. It is known that higher degree defects are unstable [28] for the one constant Frank model of nematic LCs. However in LCNs, higher degree defects do not split apart due to the constraining nature of the polymer network. We refer to [4] for blueprinted defects with degrees up to order 10 in LCNs.

The scaling of thickness in models of thin 3D elastic bodies dictates 2D models of LCNs/LCEs. If the energy is scaled linearly with the thickness, the resulting model is a membrane model: the energy is a function of the first fundamental form of the deformed surface and encodes stretching. Works that studied membrane models include [19, 25, 29]. For LCNs, the first fundamental form of zero stretching energy states satisfy a pointwise metric condition. Extensive work dedicated to examining configurations that satisfy this metric condition include [30, 31, 32, 33, 34, 10, 35, 36, 37]. For a review of these techniques, we refer to [11]. The second common scaling is a cubic scaling in the thickness, and results in a plate model driven by bending. The metric condition giving zero stretching energy becomes a constraint in the bending model. Some existing bending models include theory derived via formal asymptotics [25], a von Karman plate model derived in [38] using asymptotics, a rigorous Gamma convergence theory for a model of bilayer materials composed of LCEs and a classical isotropic elastic plate [24], or a plate model where the LC dramatically changes its orientation through the thickness [39]. Moreover, reduced 1D models for LCNs/LCEs have been explored as well; we refer to [40] for a rod model and to [41, 42] for ribbon models.

Computation of LCEs/LCNs have received some attention. Publications include computations of various membrane models [34], a membrane model with regularization [26], a bending model of LCE bilayer structure [24], a relevant 2D model for LCEs [22], 3D models [43, 44], and LCE rods [40]. Literature involving numerical analysis is limited, to the best of our knowledge. Paper [22] proves well-posedness of a mixed method for a 2D model with Frank-Oseen regularization. Our companion paper [45] provides a numerical analysis of the finite element method (FEM) described in this article. This paper also derives the LCN model and properties of solutions via formal asymptotics and presents numerous simulations of practical interest. We refer to Section 1.4 for a list of our main contributions and outline.

1.1. 3D elastic energy: Neo-classical energy. We are concerned with thin films of LCNs, and mathematically slender materials are usually modeled as 3D hyper-elastic bodies $\mathcal{B} := \Omega \times (-t/2, t/2)$, with $\Omega \subset \mathbb{R}^2$ being a bounded Lipschitz domain and $t > 0$ being a small thickness parameter. We denote by $\mathbf{u} : \mathcal{B} \rightarrow \mathbb{R}^3$ the 3D deformation of the LCNs material.

The neo-classical energy density for incompressible nematic elastomers/networks has been proposed by Bladon, Warner and Terentjev in [15, 16, 17] and reads

$$(1) \quad W_{3D}(\mathbf{x}, \mathbf{F}) := \text{tr}(\mathbf{F}^T \mathbf{L}_n^{-1} \mathbf{F} \mathbf{L}_m) - 3,$$

where $\mathbf{x} := (\mathbf{x}', x_3) := (x_1, x_2, x_3) \in \mathcal{B}$ is the space variable and $\mathbf{F} := \nabla \mathbf{u} \in \mathbb{R}^{3 \times 3}$ is the deformation gradient. We define by $\mathbf{m} : \mathcal{B} \rightarrow \mathbb{S}^2$ the *blueprinted* nematic director field on the reference configuration. The director field $\mathbf{n} : \mathcal{B} \rightarrow \mathbb{S}^2$ is the director field on the deformed configuration, to be defined below, whereas

$$(2) \quad L_{\mathbf{m}} := (s_0 + 1)^{-1/3} (I_3 + s_0 \mathbf{m} \otimes \mathbf{m})$$

is the reference step length tensor, and

$$(3) \quad L_{\mathbf{n}} := (s + 1)^{-1/3} (I_3 + s \mathbf{n} \otimes \mathbf{n})$$

is the current step length tensor. These step length tensors measure the anisotropy contributed by nematogenic molecular units to nematic elastomers/networks, which are isotropic solids with a fluid-like anisotropic ordering. Moreover, $s_0, s \in L^\infty(\Omega)$ are nematic order parameters that refer to the *reference* configuration and *deformed* configuration respectively. They are typically constant and depend on temperature, but may vary in Ω if the liquid crystal polymers are actuated non-uniformly by a light source. These parameters have a physical range

$$-1 < s_0, s \leq C < \infty.$$

We emphasize that the energy density $W_{3D}(\mathbf{x}, \mathbf{F})$ defined in (1) depends explicitly on coordinates \mathbf{x} , due to the dependence of $\mathbf{m}, \mathbf{n}, s, s_0$ on \mathbf{x} .

The energy can be rewritten as the neo-Hookean energy density:

$$(4) \quad W_{3D}(\mathbf{x}, \mathbf{F}) = |\mathbf{L}_{\mathbf{n}}^{-1/2} \mathbf{F} \mathbf{L}_{\mathbf{m}}^{1/2}|^2 - 3.$$

In the case where $s = s_0 = 0$, the step length tensors become $L_{\mathbf{m}} = L_{\mathbf{n}} = I_3$, the identity matrix $I_3 \in \mathbb{R}^{3 \times 3}$, and the formula (4) reduces to the classical neo-Hookean energy density for rubber-like materials $W_{3D}(\mathbf{F}) = |\mathbf{F}|^2 - 3$. Moreover, the material is assumed to be incompressible, i.e.,

$$(5) \quad \det \mathbf{F} = 1.$$

The 3D energy density W_{3D} is *non-degenerate*, namely

$$(6) \quad W_{3D}(\mathbf{x}, \mathbf{F}) \geq \text{dist}(\mathbf{L}_{\mathbf{n}}^{-1/2} \mathbf{F} \mathbf{L}_{\mathbf{m}}^{1/2}, SO(3))^2 \geq 0$$

for all $\mathbf{F} \in \mathbb{R}^{3 \times 3}$ such that $\det \mathbf{F} = 1$. We refer to [23, Appendix A] and [45] for a proof of this fundamental property.

Recall that the density of crosslinks between the mesogens and polymer network differentiate LCNs (also called liquid crystal glasses) and liquid crystals elastomers (LCEs): the former has moderate to dense crosslinks, while in the latter the density of crosslinks is low [9]. In this paper, we focus on LCNs and leave a numerical study of LCEs for future research. Mathematically, the strong coupling in LCNs is reflected in terms of director fields via a *kinematic constraint* [25]:

$$(7) \quad \mathbf{n} := \frac{\mathbf{F} \mathbf{m}}{|\mathbf{F} \mathbf{m}|}.$$

This implies that, in contrast to LCEs [16, 24], \mathbf{n} is *not* a free variable for models of LCNs; in fact it is also called frozen director [26]. For LCEs the energy density may be minimized over \mathbf{n} first and next over \mathbf{F} , like in [19, 43], or a Frank elastic energy for \mathbf{n} may be introduced (c.f. [21, 24, 22]). Moreover, we note that a director field description may not be the only choice for modeling LC components. One can also formulate a model with Q -tensor descriptions like in [46].

Using the energy density (1), or equivalently (4), the 3D elastic energy is given by

$$(8) \quad E_{3D}[\mathbf{u}] = \int_{\Omega} \int_{-t/2}^{t/2} W_{3D}(\mathbf{x}, \nabla \mathbf{u}) d\mathbf{x}' dx_3,$$

where $\mathbf{x}' \in \Omega$, $x_3 \in (-t/2, t/2)$, and $\det \nabla \mathbf{u} = 1$.

1.2. Model reduction. We assume the 3D director field $\mathbf{m} : \mathcal{B} \rightarrow \mathbb{S}^2$ is planar and it depends only on \mathbf{x}' , and therefore, with a slightly abuse of notations, we define $\mathbf{m} : \Omega \rightarrow \mathbb{S}^1$ to be the 2D *blueprinted* director field. We denote by $\mathbf{y} : \Omega \rightarrow \mathbb{R}^3$ the 3D deformation of the 2D midplane Ω .

The 2D membrane model is the following minimization problem: find $\mathbf{y}^* \in H^1(\Omega; \mathbb{R}^3)$ that solves

$$(9) \quad \mathbf{y}^* \in \operatorname{argmin}_{\mathbf{y} \in H^1(\Omega; \mathbb{R}^3)} E_{str}[\mathbf{y}], \quad E_{str}[\mathbf{y}] := \int_{\Omega} W_{str}(\mathbf{x}', \nabla \mathbf{y}) d\mathbf{x}',$$

where W_{str} is a stretching energy density that is only a function of $\mathbf{x}' \in \Omega$ and the first fundamental form $\mathbf{I}[\mathbf{y}] = \nabla \mathbf{y}^T \nabla \mathbf{y}$. It is defined as

$$(10) \quad W_{str}(\mathbf{x}', \nabla \mathbf{y}) := \lambda \left[\frac{1}{J[\mathbf{y}]} + \frac{1}{s+1} \left(\operatorname{tr}(\mathbf{I}[\mathbf{y}]) + s_0 C_{\mathbf{m}}[\mathbf{y}] + s \frac{J[\mathbf{y}]}{C_{\mathbf{m}}[\mathbf{y}]} \right) \right] - 3,$$

where the *actuation parameter* $\lambda : \Omega \rightarrow \mathbb{R}^+$ is given and well-defined by

$$(11) \quad \lambda = \lambda_{s,s_0} := \sqrt[3]{\frac{s+1}{s_0+1}},$$

because $s, s_0 > -1$. If the material is heated, then $\lambda < 1$, whereas if it is cooled, then $\lambda > 1$. Moreover, $J[\mathbf{y}], C_{\mathbf{m}}[\mathbf{y}]$ are among the following abbreviations:

$$(12) \quad J[\mathbf{y}] = \det \mathbf{I}[\mathbf{y}], \quad C_{\mathbf{m}}[\mathbf{y}] = \mathbf{m} \cdot \mathbf{I}[\mathbf{y}] \mathbf{m}, \quad C_{\mathbf{m}_{\perp}}[\mathbf{y}] = \mathbf{m}_{\perp} \cdot \mathbf{I}[\mathbf{y}] \mathbf{m}_{\perp}.$$

We employ a similar notation when the second argument of W_{str} is $\mathbf{F} \in \mathbb{R}^{3 \times 2}$

$$(13) \quad \begin{aligned} \mathbf{I}(\mathbf{F}) &:= \mathbf{F}^T \mathbf{F}, \quad J(\mathbf{F}) := \det \mathbf{I}(\mathbf{F}), \\ C_{\mathbf{m}}(\mathbf{F}) &:= \mathbf{m} \cdot \mathbf{I}(\mathbf{F}) \mathbf{m}, \quad C_{\mathbf{m}_{\perp}}(\mathbf{F}) := \mathbf{m}_{\perp} \cdot \mathbf{I}(\mathbf{F}) \mathbf{m}_{\perp}. \end{aligned}$$

We also define the first order variational derivative of $\mathbf{I}[\mathbf{y}]$ along \mathbf{v} as

$$(14) \quad K[\mathbf{y}, \mathbf{v}] := \delta \mathbf{I}[\mathbf{y}](\mathbf{v}) = \nabla \mathbf{y}^T \nabla \mathbf{v} + \nabla \mathbf{v}^T \nabla \mathbf{y},$$

for later use. We emphasize that since s, s_0, \mathbf{m} depends on $\mathbf{x}' \in \Omega$ then W_{str} also has an explicit dependence on \mathbf{x}' .

We note that (10) is consistent with the stretching energy in [25] after additionally assuming an inextensibility constraint $J[\mathbf{y}] = 1$ and up to the multiplicative parameter λ and the constant -3 .

The energy density (10) lacks quasi-convexity, the correct notion of convexity for a vector-valued problem. This is responsible for the main difficulties to prove convergence of our discretization as well as to design efficient iterative solvers for the discrete minimization problem. We discuss convergence of discrete minimizers in [45], and present an iterative scheme in Section 4.3.

Throughout this work, we do not impose any boundary condition so that the material under consideration has *free boundaries*. If necessary, one can take Dirichlet boundary conditions into account with a simple modification on the method.

An important property of the stretching energy is that $W_{str}(\mathbf{x}', \nabla \mathbf{y}) = 0$ if and only if $\mathbb{I}[\mathbf{y}] = g$ pointwise, where $g \in \mathbb{R}^{2 \times 2}$ is the *target metric*

$$(15) \quad g = \lambda^2 \mathbf{m} \otimes \mathbf{m} + \lambda^{-1} \mathbf{m}_\perp \otimes \mathbf{m}_\perp;$$

we show this property in Section 2.3. In the physics literature, maps \mathbf{y} that satisfy the metric constraint $\mathbb{I}[\mathbf{y}] = g$ are known as spontaneous distortions [16, 30]. The physics community has developed techniques to find such deformations in *special situations*. Some examples are radially symmetric director fields [35], cylindrical shapes [36], and nonisometric origami [10, 23, 32, 33]. We refer to [11] for a review of the techniques to predict shapes based on the metric. The purpose of this work is to provide a different approach via energy minimization and approximation. Rather than constructing \mathbf{y} analytically such that $\mathbb{I}[\mathbf{y}] = g$, we numerically approximate minimizers to the stretching energy, which suits more general situations.

1.3. Discretizations. In this work, we propose a FEM discretization to (9). We consider the space \mathbb{V}_h of continuous piecewise linear finite elements over a shape regular mesh \mathcal{T}_h , and approximate the deformation \mathbf{y} by $\mathbf{y}_h \in \mathbb{V}_h$. To define a discrete energy, we replace \mathbf{y} in (9) by \mathbf{y}_h and then add a *regularization* term

$$(16) \quad R_h[\mathbf{y}_h] := c_r h^2 \sum_{e \in \mathcal{E}_h} \frac{1}{h} \int_e |\nabla \mathbf{y}_h|^2$$

to handle the lack of convexity of E . This regularization term is a scaled L^2 norm of jumps $[\nabla \mathbf{y}_h]$ across all the interior edges $e \in \mathcal{E}_h$ of \mathcal{T}_h , and provides a numerical selection mechanism to remove oscillations from equilibrium configurations; see Section 5.5. We prove convergence of discrete minimizers in our accompanying paper [45]. Moreover, we design a nonlinear gradient flow scheme with an embedded Newton sub-iteration, to solve the discrete minimization problem.

1.4. Our contributions and outline. We summarize our main contributions in this work as follows.

- **Asymptotic derivation of the 2D membrane model.** Motivated by [25], we derive the 2D membrane model from 3D rubber elasticity via an asymptotic analysis. Inspired by [26], we also connect W_{str} and W_{3D} with the notion of minimal energy extension. This is the content of Sections 2.1 and 2.2. Moreover, we show that global minimizers of (9) satisfy the target metric (36) in Section 2.3.
- **Asymptotic profiles of defects.** In Section 3, we present a new formal construction of solutions for rotationally symmetric blueprinted director fields \mathbf{m} with a defect of degree $n > 1$. Our technique hinges on the ideas of lifted surfaces (inspired by [23]), composition of defects and Taylor expansion.
- **A new finite element discretization and iterative solver.** In Section 4, we devise our finite element discretization of (9) that includes the regularization term (16), as well as a nonlinear gradient flow scheme together with a Newton sub-iteration to solve the resulting discrete nonconvex minimization problem. We prove that our scheme is an energy descent method. We also show well-posedness and convergence of the Newton sub-iteration provided the pseudo time step τ is moderately small relative to the meshsize h and the previous iterate satisfies a suitable but plausible regularity assumption; proofs are given in the Appendix A.

- **Numerical simulations.** In Section 5, we present numerous simulations of practical interest. They illustrate the effectiveness of our method and features of this membrane model. In fact, they document that the algorithm and model can capture intriguing physical phenomena such as origami-like structures and deformations due to defects with varying degree. Our simulations also reveal the roles of parameters s, s_0 in the model, and the effect of regularization.

2. MEMBRANE MODEL OF LIQUID CRYSTALS POLYMER NETWORKS

In this section, we introduce a formal asymptotic derivation of a membrane model of LCNs, discuss properties of the model related to its global minimizers, and present a technique for formal construction of solution profiles with defects.

2.1. Derivation of stretching energy from asymptotics. This section is dedicated to deriving a 2D stretching or membrane energy from (8) via formal asymptotics as the thickness t goes to zero. In particular, we shall derive the formal limit $\lim_{t \rightarrow 0} \frac{1}{t} E_{3D}[\mathbf{u}]$. This procedure will follow closely the derivation of [25], but we will relax the simplifying assumption $\det \mathbf{I}[\mathbf{y}] = 1$ made in [25]. We also contrast the asymptotic method presented here with the more analytical method presented in [26]. The connection between the two will be explored in Section 2.2.

2.1.1. Kirchhoff-Love assumption and overview of strategy. We assume that the 3D deformation $\mathbf{u} : \mathcal{B} := \Omega \times (-t/2, t/2) \rightarrow \mathbb{R}^3$ takes the form

$$(17) \quad \mathbf{u}(\mathbf{x}', x_3) = \mathbf{y}(\mathbf{x}') + \phi(\mathbf{x}', x_3) \boldsymbol{\nu}(\mathbf{x}')$$

where $\mathbf{y} : \Omega \rightarrow \mathbb{R}^3$ is the reduced deformation and $\boldsymbol{\nu} : \Omega \rightarrow \mathbb{R}^3$ is the normal to the deformed midplane $\mathbf{y}(\Omega)$. We posit that ϕ takes the form:

$$(18) \quad \phi(\mathbf{x}', x_3) = \alpha(\mathbf{x}') x_3 + \mathcal{O}(x_3^2),$$

which is a modified *Kirchhoff-Love assumption*. The higher order terms would be useful for deriving the bending energy, but we do not need them for the stretching energy. Note that α is undetermined for the moment. Later, α will be chosen so that \mathbf{u} is incompressible in an asymptotic sense, i.e. $\det \nabla \mathbf{u}(\mathbf{x}', x_3) = 1 + \mathcal{O}(x_3)$.

The goal of asymptotics is to write the energy $W_{3D}(\mathbf{x}, \nabla \mathbf{u})$ given in (1) for the deformation \mathbf{u} in terms of powers of t and the reduced stretching energy $W_{str}(\mathbf{x}', \nabla' \mathbf{y})$

$$(19) \quad \int_{-t/2}^{t/2} \int_{\Omega} W_{3D}(\mathbf{x}, \nabla \mathbf{u}) d\mathbf{x}' dx_3 = t \int_{\Omega} W_{str}(\mathbf{x}', \nabla' \mathbf{y}) d\mathbf{x}' + \mathcal{O}(t^3),$$

where $\nabla' := (\partial_1, \partial_2)$ denotes the gradient with respect to \mathbf{x}' . The stretching energy W_{str} in (19) gives the leading order effects of the energy as the body thickness t vanishes in the sense that formally

$$\lim_{t \rightarrow 0} \frac{1}{t} \int_{-t/2}^{t/2} \int_{\Omega} W_{3D}(\mathbf{x}, \nabla \mathbf{u}) d\mathbf{x}' dx_3 = \int_{\Omega} W_{str}(\mathbf{x}', \nabla' \mathbf{y}) d\mathbf{x}'.$$

The third order term in (19) corresponds to the bending energy W_{ben} and is not the focus of the current work. Combined with the modified Kirchhoff-Love assumption (17), the process to derive the stretching energy is as follows:

- (1) Write the Cauchy tensor $\mathbf{C} = \mathbf{F}^T \mathbf{F}$ in terms of leading order terms.
- (2) Write W_{3D} in terms of \mathbf{C} and powers of x_3 .
- (3) Collect $\mathcal{O}(1)$ terms of W_{3D} which contribute to the stretching energy.
- (4) Determine α so that \mathbf{u} satisfies incompressibility in an asymptotic sense.

2.1.2. *Cauchy tensor.* Substituting (17) into $\mathbf{C} := \nabla \mathbf{u}^T \nabla \mathbf{u}$ yields

$$(20) \quad \mathbf{C} = \nabla \mathbf{u}^T \nabla \mathbf{u} = \begin{bmatrix} \mathbf{C}_\phi & \mathbf{C}_{1 \times 2}^T \\ \mathbf{C}_{1 \times 2} & \mathbf{C}_{1 \times 1} \end{bmatrix},$$

where

$$(21) \quad \mathbf{C}_\phi = \nabla' \mathbf{y}^T \nabla' \mathbf{y} + \phi (\nabla' \boldsymbol{\nu}^T \nabla' \mathbf{y} + \nabla' \mathbf{y}^T \nabla' \boldsymbol{\nu}) + \phi^2 \nabla' \boldsymbol{\nu}^T \nabla' \boldsymbol{\nu} + \nabla' \phi \otimes \nabla' \phi$$

$$(22) \quad \mathbf{C}_{1 \times 2} = (\boldsymbol{\nu} \otimes \nabla' \phi)^T \partial_3 \phi \boldsymbol{\nu} = \partial_3 \phi \nabla' \phi$$

$$(23) \quad \mathbf{C}_{1 \times 1} = (\partial_3 \phi)^2.$$

Here, we have used the facts that $\nabla' \mathbf{y}^T \boldsymbol{\nu} = 0$, $\nabla' \boldsymbol{\nu}^T \boldsymbol{\nu} = 0$ and $|\boldsymbol{\nu}| = 1$. Since $\nabla' \phi(\mathbf{x}', x_3) = \nabla' \alpha x_3 + \mathcal{O}(x_3^2)$ and $\partial_3 \phi(\mathbf{x}', x_3) = \alpha + \mathcal{O}(x_3)$, we have $\mathbf{C}_{1 \times 2} = \mathcal{O}(x_3)$, and hence we may drop $\mathbf{C}_{1 \times 2}$ as higher order terms.

Also ignoring any terms higher than constant order, we have

$$\mathbf{C}_\phi = \mathbf{I}[\mathbf{y}] + \mathcal{O}(x_3),$$

where $\mathbf{I}[\mathbf{y}] = \nabla' \mathbf{y}^T \nabla' \mathbf{y}$ is the first fundamental form of \mathbf{y} . Since

$$(\partial_3 \phi(\mathbf{x}', x_3))^2 = \alpha(\mathbf{x}')^2 + \mathcal{O}(x_3),$$

we find

$$(24) \quad \mathbf{C} = \begin{bmatrix} \mathbf{I}[\mathbf{y}] & 0 \\ 0 & \alpha(\mathbf{x}')^2 \end{bmatrix} + \mathcal{O}(x_3).$$

2.1.3. *Expanding W_{3D} .* Recall that we assume that the 3D blueprinted director field \mathbf{m} lies in the plane i.e.

$$(25) \quad \mathbf{m}(\mathbf{x}) = (\tilde{\mathbf{m}}(\mathbf{x}'), 0)^T.$$

First, substituting the kinematic constraint (7) into (1) with $\mathbf{F} = \nabla \mathbf{u}$, we obtain

$$(26) \quad W_{3D}(\mathbf{x}', \nabla \mathbf{u}) = \lambda \left(\text{tr } \mathbf{C} + \frac{s_0}{s+1} \mathbf{m} \cdot \mathbf{C} \mathbf{m} - \frac{s}{s+1} \frac{\mathbf{m} \cdot \mathbf{C}^2 \mathbf{m}}{\mathbf{m} \cdot \mathbf{C} \mathbf{m}} \right) - 3,$$

where λ is defined in (11), and we notice that from now on W_{3D} depends on \mathbf{x}' instead of \mathbf{x} , due to the assumption (25). Then plugging the asymptotic form (24) of \mathbf{C} into (26) and using (25), the energy density $W_{3D}(\mathbf{x}', \nabla \mathbf{u})$ becomes

$$\begin{aligned} W_{3D}(\mathbf{x}', \nabla \mathbf{u}) &= \lambda \left[\text{tr } \mathbf{I}[\mathbf{y}] + \alpha(\mathbf{x}')^2 + \frac{s_0}{s+1} \tilde{\mathbf{m}} \cdot \mathbf{I}[\mathbf{y}] \tilde{\mathbf{m}} - \frac{s}{s+1} \frac{\tilde{\mathbf{m}} \cdot \mathbf{I}[\mathbf{y}]^2 \tilde{\mathbf{m}}}{\tilde{\mathbf{m}} \cdot \mathbf{I}[\mathbf{y}] \tilde{\mathbf{m}}} \right] - 3 + \mathcal{O}(x_3). \end{aligned}$$

Since $\mathbf{I}[\mathbf{y}]$ is a 2×2 matrix, the Caley-Hamilton Theorem gives

$$\mathbf{I}[\mathbf{y}]^2 = (\text{tr } \mathbf{I}[\mathbf{y}]) \mathbf{I}[\mathbf{y}] - \det \mathbf{I}[\mathbf{y}] \mathbf{I}_2,$$

so that the energy now reads

$$\begin{aligned} W_{3D}(\mathbf{x}', \nabla \mathbf{u}) &= \lambda \left[\alpha(\mathbf{x}')^2 + \frac{1}{s+1} \left(\text{tr } \mathbf{I}[\mathbf{y}] + s_0 \tilde{\mathbf{m}} \cdot \mathbf{I}[\mathbf{y}] \tilde{\mathbf{m}} + s \frac{\det \mathbf{I}[\mathbf{y}]}{\tilde{\mathbf{m}} \cdot \mathbf{I}[\mathbf{y}] \tilde{\mathbf{m}}} \right) \right] - 3 + \mathcal{O}(x_3). \end{aligned}$$

We now have all the constant order terms of $W_{3D}(\mathbf{x}', \nabla \mathbf{u})$. The only remaining task is to determine $\alpha(\mathbf{x}')$. We do this next.

2.1.4. *Incompressibility.* Since we would like \mathbf{u} to satisfy incompressibility $\det \nabla \mathbf{u} = 1 + \mathcal{O}(x_3)$, we impose $\det \mathbf{C} = 1 + \mathcal{O}(x_3)$. By (24), we see that

$$(27) \quad \det \mathbf{C} = \det \mathbf{I}[\mathbf{y}] \alpha(\mathbf{x}')^2 + \mathcal{O}(x_3),$$

whence

$$(28) \quad \alpha(\mathbf{x}') = \frac{1}{\sqrt{\det \mathbf{I}[\mathbf{y}]}}$$

gives us the desired equality $\det \mathbf{C} = 1 + \mathcal{O}(x_3)$. This further implies

$$(29) \quad \nabla \mathbf{u} = [\nabla \mathbf{y}, (\det \mathbf{I}[\mathbf{y}])^{-1/2} \boldsymbol{\nu}] + \mathcal{O}(x_3).$$

2.1.5. *Stretching energy.* For convenience of presentation, from now on we slightly abuse notation and drop the prime for ∇' and tilde for $\tilde{\mathbf{m}}$. Therefore, we will denote

$$(30) \quad \mathbf{m} = \tilde{\mathbf{m}} \in \mathbb{R}^2, \quad \mathbf{m} = (\tilde{\mathbf{m}}, 0)^T \in \mathbb{R}^3$$

depending on whether we regard \mathbf{m} as a vector in \mathbb{R}^2 or \mathbb{R}^3 .

We conclude that, with the steps built in Sections 2.1.1-2.1.4, we finally derive the stretching energy in (10).

2.2. **Minimal energy extension.** In this section we show that the stretching energy density (10) is the minimal energy extension of the 3D energy (1). The proof is similar to that of [19, Lemma 5.3] and is related to how [26] derives the model.

Proposition 1 (minimal energy extension). *Let $\mathbf{F} \in \mathbb{R}^{3 \times 2}$ have rank 2. We have the following equality between W_{str} defined in (10) and W_{3D} given in (1)*

$$(31) \quad W_{str}(\mathbf{x}', \mathbf{F}) = \inf_{\mathbf{b} \in \mathbb{R}^3: \det[\mathbf{F}, \mathbf{b}] = 1} W_{3D}(\mathbf{x}', [\mathbf{F}, \mathbf{b}]).$$

Moreover, the unique minimizer \mathbf{b} is

$$(32) \quad \frac{\mathbf{F}_1 \times \mathbf{F}_2}{|\mathbf{F}_1 \times \mathbf{F}_2|^2} =: \operatorname{argmin}_{\mathbf{b} \in \mathbb{R}^3: \det[\mathbf{F}, \mathbf{b}] = 1} W_{3D}(\mathbf{x}', [\mathbf{F}, \mathbf{b}]),$$

where $\mathbf{F}_1, \mathbf{F}_2$ are columns of \mathbf{F} .

Proof. The incompressibility constraint reads $\det[\mathbf{F}, \mathbf{b}] = \mathbf{b}^T(\mathbf{F}_1 \times \mathbf{F}_2) = 1$. Using (26) and (30) to determine $W_{3D}(\mathbf{x}', [\mathbf{F}, \mathbf{b}])$ for $\mathbf{b} \in \mathbb{R}^3$ yields

$$W_{3D}(\mathbf{x}', [\mathbf{F}, \mathbf{b}]) = \lambda \left(\operatorname{tr} \mathbf{I}(\mathbf{F}) + |\mathbf{b}|^2 + \frac{s_0}{s+1} C_{\mathbf{m}}(\mathbf{F}) - \frac{s}{s+1} \frac{|\mathbf{I}(\mathbf{F})\mathbf{m}|^2 + (\mathbf{b} \cdot \mathbf{F}\mathbf{m})^2}{C_{\mathbf{m}}(\mathbf{F})} \right) - 3.$$

If we append the term $\mu(\mathbf{b}^T(\mathbf{F}_1 \times \mathbf{F}_2) - 1)$ to $W_{3D}(\mathbf{x}', [\mathbf{F}, \mathbf{b}])$, with Lagrange multiplier μ , we see that \mathbf{b} and μ solve the following saddle point system

$$\begin{pmatrix} 2\lambda \left(I_3 - \frac{s}{(s+1)C_{\mathbf{m}}(\mathbf{F})} \mathbf{F}\mathbf{m} \otimes \mathbf{F}\mathbf{m} \right) & \mathbf{F}_1 \times \mathbf{F}_2 \\ (\mathbf{F}_1 \times \mathbf{F}_2)^T & 0 \end{pmatrix} \begin{pmatrix} \mathbf{b} \\ \mu \end{pmatrix} = \begin{pmatrix} 0 \\ 1 \end{pmatrix},$$

whose unique solution is $\mathbf{b} = (\mathbf{F}_1 \times \mathbf{F}_2)/|\mathbf{F}_1 \times \mathbf{F}_2|^2$ and $\mu = -\frac{2\lambda}{|\mathbf{F}_1 \times \mathbf{F}_2|^2}$. Note that the uniqueness of \mathbf{b} follows from the invertibility of the upper-left 3×3 block matrix, which follows from the fact that $\frac{s}{s+1} < 1$. Since $|\mathbf{F}_1 \times \mathbf{F}_2|^2 = \det \mathbf{I}(\mathbf{F}) = J(\mathbf{F})$, substituting the minimizing \mathbf{b} into the 3D energy yields

$$(33) \quad W_{3D}(\mathbf{x}', [\mathbf{F}, \mathbf{b}]) = \lambda \left(\operatorname{tr} \mathbf{I}(\mathbf{F}) + \frac{1}{J(\mathbf{F})} + \frac{s_0}{s+1} C_{\mathbf{m}}(\mathbf{F}) - \frac{s}{s+1} \frac{|\mathbf{I}(\mathbf{F})\mathbf{m}|^2}{C_{\mathbf{m}}(\mathbf{F})} \right) - 3.$$

Applying the Cayley Hamilton Theorem for a 2×2 matrix \mathbf{A} , namely $\mathbf{A}^2 - \text{tr}(\mathbf{A})\mathbf{A} + (\det \mathbf{A})I_2 = \mathbf{0}$, to the last term inside bracket on the RHS of (33) yields

$$(34) \quad \frac{|\mathbf{I}(\mathbf{F})\mathbf{m}|^2}{C_{\mathbf{m}}(\mathbf{F})} = \frac{\mathbf{m} \cdot \mathbf{I}(\mathbf{F})^2 \mathbf{m}}{C_{\mathbf{m}}(\mathbf{F})} = \text{tr} \mathbf{I}(\mathbf{F}) - \frac{J(\mathbf{F})}{C_{\mathbf{m}}(\mathbf{F})}.$$

We then insert (34) into the RHS of (33) to obtain

$$W_{3D}(\mathbf{x}', [\mathbf{F}, \mathbf{b}]) = \lambda \left(\frac{1}{J(\mathbf{F})} + \frac{1}{s+1} \left[\text{tr} \mathbf{I}(\mathbf{F}) + s_0 C_{\mathbf{m}}(\mathbf{F}) + s \frac{J(\mathbf{F})}{C_{\mathbf{m}}(\mathbf{F})} \right] \right) - 3 = W_{str}(\mathbf{x}', \mathbf{F}),$$

which is the desired equality. \square

Remark 1 (asymptotics vs minimal energy extension). If $\mathbf{F} = \nabla \mathbf{y}$, then the minimizing \mathbf{b} in Proposition 1 is

$$\mathbf{b} = \frac{\boldsymbol{\nu}}{\sqrt{\det I[\mathbf{y}]}},$$

This corroborates that the asymptotic expression (29) gives the correct extension. However, this formula for \mathbf{b} relies on the fact that \mathbf{m} is planar; see (30). If \mathbf{m} were not planar, then the formula for \mathbf{b} would be more complicated. We refer to [23].

The next corollary is an easy consequence of Proposition 1 and (6).

Corollary 1 (nondegeneracy). *The stretching energy $W_{str}(\mathbf{F})$ satisfies*

$$(35) \quad W_{str}(\mathbf{x}', \mathbf{F}) \geq \text{dist}(\mathbf{L}_{\mathbf{n}}^{-1/2}[\mathbf{F}, \mathbf{b}] \mathbf{L}_{\mathbf{m}}^{1/2}, SO(3))^2 \geq 0$$

for all $\mathbf{F} \in \mathbb{R}^{3 \times 2}$ such that $\text{rank}(\mathbf{F}) = 2$ and $\mathbf{b} = \frac{\mathbf{F}_1 \times \mathbf{F}_2}{|\mathbf{F}_1 \times \mathbf{F}_2|^2}$.

2.3. Global minimizers and target metrics. In this section, we characterize global minimizers of (9). We show that minimizing the stretching energy density W_{str} is equivalent to satisfying the target metric constraint pointwise. We point to [23, Appendix A] for a similar result, but for a related 3 dimensional model.

Proposition 2 (target metric). *The stretching energy density $W_{str}(\mathbf{x}', \mathbf{F}) = 0$ vanishes at $\mathbf{F} \in \mathbb{R}^{3 \times 2}$ if and only if $\mathbf{I}(\mathbf{F}) = g$ where $g \in \mathbb{R}^{2 \times 2}$ is given by*

$$(36) \quad g = \lambda^2 \mathbf{m} \otimes \mathbf{m} + \lambda^{-1} \mathbf{m}_{\perp} \otimes \mathbf{m}_{\perp},$$

λ is defined in (11) and $\mathbf{m}_{\perp} : \Omega \rightarrow \mathbb{S}^1$ is perpendicular to \mathbf{m} .

Proof. First suppose that $\mathbf{I}(\mathbf{F}) = g$. Inserting (36) into (10) gives

$$\begin{aligned} W_{str}(\mathbf{x}', \mathbf{F}) &= \lambda \left(\frac{1}{\det g} + \frac{1}{s+1} \left(\text{tr} g + s_0 \mathbf{m} \cdot g \mathbf{m} + s \frac{\det g}{\mathbf{m} \cdot g \mathbf{m}} \right) \right) - 3 \\ &= \lambda \left(\lambda^{-1} + \frac{1}{s+1} \left(\lambda^2 + \lambda^{-1} + s_0 \lambda^2 + s \lambda^{-1} \right) \right) - 3 \\ &= \lambda \left(\lambda^{-1} + \frac{1}{s+1} \left((s_0 + 1) \lambda^2 + (s + 1) \lambda^{-1} \right) \right) - 3 \\ &= \lambda \left(2\lambda^{-1} + \frac{s_0 + 1}{s+1} \lambda^2 \right) - 3. \end{aligned}$$

Note that $\frac{s_0 + 1}{s+1} = \lambda^{-3}$, whence

$$W_{str}(\mathbf{x}', \mathbf{F}) = \lambda \left(2\lambda^{-1} + \lambda^{-3} \lambda^2 \right) - 3 = 0.$$

Now suppose that $W_{str}(\mathbf{x}', \mathbf{F}) = 0$. Corollary 1 (nondegeneracy) guarantees

$$0 = W_{str}(\mathbf{x}', \mathbf{F}) \geq \text{dist}(\mathbf{L}_n^{-1/2}[\mathbf{F}, \mathbf{b}]\mathbf{L}_m^{1/2}, SO(3))^2 \geq 0,$$

for $\mathbf{b} = \frac{\mathbf{F}_1 \times \mathbf{F}_2}{|\mathbf{F}_1 \times \mathbf{F}_2|^2}$. This implies there is a rotation $\mathbf{R} \in SO(3)$ such that

$$\mathbf{L}_n^{-1/2}[\mathbf{F}, \mathbf{b}]\mathbf{L}_m^{1/2} = \mathbf{R}.$$

Multiplying both sides by \mathbf{R}^T yields

$$\mathbf{L}_m^{1/2}[\mathbf{F}, \mathbf{b}]^T \mathbf{L}_n^{-1}[\mathbf{F}, \mathbf{b}]\mathbf{L}_m^{1/2} = I_3.$$

We shall now perform some algebraic operations to determine what $\mathbf{I}(\mathbf{F}) = \mathbf{F}^T \mathbf{F}$ should satisfy. First, multiplying on the left and right by $\mathbf{L}_m^{-1/2}$ gives

$$[\mathbf{F}, \mathbf{b}]^T \mathbf{L}_n^{-1}[\mathbf{F}, \mathbf{b}] = \mathbf{L}_m^{-1}.$$

The definitions (2) and (3) of \mathbf{L}_m and \mathbf{L}_n , with $\mathbf{m} \in \mathbb{R}^3$ given by (30), imply

$$\mathbf{L}_m^{-1} = (s_0 + 1)^{1/3} \left(I_3 - \frac{s_0}{s_0 + 1} \mathbf{m} \otimes \mathbf{m} \right), \quad \mathbf{L}_n^{-1} = (s + 1)^{1/3} \left(I_3 - \frac{s}{s + 1} \mathbf{n} \otimes \mathbf{n} \right),$$

and combined with the kinematic constraint $\mathbf{n} = \frac{\mathbf{F}\mathbf{m}}{|\mathbf{F}\mathbf{m}|}$, this further yields

$$(37) \quad \begin{aligned} \mathbf{L}_m^{-1} = [\mathbf{F}, \mathbf{b}]^T \mathbf{L}_n^{-1}[\mathbf{F}, \mathbf{b}] &= (s + 1)^{1/3} \begin{pmatrix} \mathbf{I}(\mathbf{F}) & 0 \\ 0 & \frac{1}{J(\mathbf{F})} \end{pmatrix} \\ &\quad - \frac{s}{(s + 1)^{2/3} C_m(\mathbf{F})} \begin{pmatrix} \mathbf{I}(\mathbf{F})\mathbf{m} \otimes \mathbf{I}(\mathbf{F})\mathbf{m} & 0 \\ 0 & 0 \end{pmatrix}. \end{aligned}$$

We express $\mathbf{I}(\mathbf{F})$ in terms of the orthonormal basis $\mathbf{m}, \mathbf{m}_\perp \in \mathbb{R}^2$ and scalars a_1, a_2, a_3

$$\mathbf{I}(\mathbf{F}) = a_1 \mathbf{m} \otimes \mathbf{m} + a_2 \mathbf{m}_\perp \otimes \mathbf{m}_\perp + a_3 (\mathbf{m}_\perp \otimes \mathbf{m} + \mathbf{m} \otimes \mathbf{m}_\perp).$$

We also extend \mathbf{m} to \mathbb{R}^3 , according to (30), and represent \mathbf{L}_m^{-1} on the orthonormal basis $(\mathbf{m}, 0)^T, (\mathbf{m}_\perp, 0)^T, \mathbf{e}_3$ of \mathbb{R}^3 . We next compare the upper-left 2×2 blocks of the matrix representations of the left and right-hand sides of (37) to obtain

$$\begin{pmatrix} (s_0 + 1)^{-2/3} & 0 \\ 0 & (s_0 + 1)^{1/3} \end{pmatrix} = (s + 1)^{1/3} \begin{pmatrix} a_1 & a_3 \\ a_3 & a_2 \end{pmatrix} - \frac{s}{(s + 1)^{2/3}} \begin{pmatrix} a_1 & a_3 \\ a_3 & a_3^2/a_1 \end{pmatrix}.$$

By matching entries, a_3 must vanish and $(s + 1)^{1/3} a_2 = (s_0 + 1)^{1/3}$, which entails that $a_2 = \left(\frac{s_0 + 1}{s + 1} \right)^{1/3} = \lambda^{-1}$. Finally,

$$(s_0 + 1)^{-2/3} = ((s + 1)^{1/3} - s(s + 1)^{-2/3}) a_1 = (s + 1)^{-2/3} a_1,$$

whence $a_1 = \left(\frac{s + 1}{s_0 + 1} \right)^{2/3} = \lambda^2$. Therefore, we get

$$\mathbf{I}(\mathbf{F}) = \lambda^2 \mathbf{m} \otimes \mathbf{m} + \lambda^{-1} \mathbf{m}_\perp \otimes \mathbf{m}_\perp = g,$$

which is the desired expression of $\mathbf{I}(\mathbf{F})$. \square

A direct consequence of the characterization of the target metric is that H^1 isometric immersions of g are minimizers to the stretching energy.

Corollary 2 (immersions of g are minimizers with vanishing energy). *A deformation $\mathbf{y} \in H^1(\Omega; \mathbb{R}^3)$ satisfies*

$$(38) \quad \mathbf{I}[\mathbf{y}] = g \text{ a.e. in } \Omega,$$

i.e., \mathbf{y} is an isometric immersion of the metric g defined in (36), if and only if \mathbf{y} is a global minimizer to (9) with $E_{str}[\mathbf{y}] = 0$.

Therefore, the solvability of (9) is related to the long standing open problem in differential geometry of existence of isometric immersions in \mathbb{R}^3 for a general metric $g : \Omega \rightarrow \mathbb{R}^{2 \times 2}$. Smooth isometric immersions in \mathbb{R}^3 are known to exist for certain metrics with positive or negative curvatures, while there are also examples of metrics that have no C^2 isometric immersions; we refer to the book [47] for discussions and further references. Corollary 2 requires the minimal regularity $\mathbf{y} \in H^1(\Omega; \mathbb{R}^3)$, but we further assume the existence of an H^2 isometric immersion to prove convergence of our FEM with regularization (16) in [45]. The existence of either H^1 or H^2 isometric immersions seems to be an open question, to the best of our knowledge. Finally, it is conceivable that g is not immersible and yet there is a global minimizer \mathbf{y} of (9) with $E_{str}[\mathbf{y}] > 0$; this justifies the requirement $E_{str}[\mathbf{y}] = 0$ in Corollary 2. We explore this matter computationally in Section 5.3.

3. ASYMPTOTIC PROFILES OF DEFECTS

We now construct asymptotic profiles for blueprinted director fields \mathbf{m} with defects of several degrees. We are not aware of studies of shapes beyond the Gauss curvature obtained in [10] for higher degree defects. Our approximate solutions provide insight on the complicated shapes that can be programmed upon actuation. We reproduce these profiles computationally later in Section 5.1.

3.1. Lifted surfaces. Lifted surfaces for LCNs/LCEs are originally introduced in [23]. We adapt the idea to the reduced model (9) in this subsection. To this end, we consider the following parameterization of lifted surfaces

$$(39) \quad \mathbf{y}^l(\mathbf{x}') = (\alpha \mathbf{x}', \phi(\alpha \mathbf{x}'))^T \quad \forall \mathbf{x}' \in \Omega,$$

where $\alpha \in \mathbb{R}$ will be determined later. Here, $\phi : \alpha\Omega \rightarrow \mathbb{R}$ represents the graph of the lifted surfaces. Our goal is to match the metric g in (36) with $\mathbf{I}[\mathbf{y}^l]$, i.e.,

$$(40) \quad \mathbf{I}[\mathbf{y}^l] = g = \lambda^2 \mathbf{m} \otimes \mathbf{m} + \lambda^{-1} \mathbf{m}_\perp \otimes \mathbf{m}_\perp = (\lambda^2 - \lambda^{-1}) \mathbf{m} \otimes \mathbf{m} + \lambda^{-1} I_2.$$

Since (39) yields

$$(41) \quad \mathbf{I}[\mathbf{y}^l] = \alpha^2 \nabla \phi(\alpha \mathbf{x}') \otimes \nabla \phi(\alpha \mathbf{x}') + \alpha^2 I_2,$$

(40) is valid if ϕ satisfies $|\nabla \phi| = \sqrt{\lambda^3 - 1}$ a.e. in Ω , and $\alpha = \lambda^{-1/2}$, with the properties that $\lambda > 1$ and λ is *constant* over Ω . Substituting them into (39) gives

$$(42) \quad \mathbf{y}^l(\mathbf{x}') = (\mathbf{x}'_\lambda, \phi(\mathbf{x}'_\lambda))^T, \quad \mathbf{x}'_\lambda := \lambda^{-1/2} \mathbf{x}'.$$

Since this deformation is an isometric immersion of the metric (36), it is also an equilibrium configuration provided $\mathbf{m}(\mathbf{x}') = \pm(\lambda^3 - 1)^{-1/2} \nabla \phi(\mathbf{x}'_\lambda)$ according to Corollary 2. We observe that the discussion so far has restricted $\lambda > 1$, which means the LCN is being cooled. If $\lambda < 1$ and ϕ satisfies $\pm \sqrt{\lambda^{-3} - 1} \nabla \phi(\lambda \mathbf{x}') = \mathbf{m}_\perp(\mathbf{x}')$, then a lifted surface of the form

$$(43) \quad \mathbf{y}^l(\mathbf{x}') = (\lambda \mathbf{x}', \phi(\lambda \mathbf{x}'))^T,$$

satisfies $I[\mathbf{y}^l] = g$. Since a lifted surface may be constructed for $\lambda < 1$ in a similar fashion as for $\lambda > 1$, we restrict the remaining discussion of this section to $\lambda > 1$. However, we note that the computations in Section 5.1 typically set $\lambda < 1$.

3.2. Surfaces for defects of degree 1 and 1/2. To set the stage, we first go over known lifted surfaces that arise from degree 1 and degree 1/2 defects. These solutions will match the metric g exactly, and will help us later in constructing approximate solutions for higher order defects in Sections 3.5 and 3.6.

A director field \mathbf{m}_1 with a defect of degree 1 reads

$$(44) \quad \mathbf{m}_1(\mathbf{x}') = \frac{\mathbf{x}'}{|\mathbf{x}'|}.$$

If \mathbf{R}_1 is a rotation of $\pm\pi/2$, the corresponding exact solution \mathbf{y}_1 for $\mathbf{R}_1\mathbf{m}_1$ reads

$$(45) \quad \mathbf{y}_1(\mathbf{x}') = \left(\mathbf{x}'_\lambda, \phi_1(\mathbf{x}'_\lambda) \right)^T$$

where

$$(46) \quad \phi_1(\mathbf{x}') = \sqrt{\lambda^3 - 1} (1 - |\mathbf{x}'|);$$

\mathbf{y}_1 is a *cone* with vertex at the origin as long as $\lambda > 1$ [30]. If $\lambda < 1$, then the cone solution in (46) is no longer well defined. In fact, the director field \mathbf{m}_1 in (44) will produce what is known as an *anticone* configuration [30]. The solution for a degree 1 defect will be a cone or anti-cone depending on the angle α_r between \mathbf{m}_1 and \mathbf{x}' as well as λ [37]. See Fig. 1 for the cone and anti-cone shapes computed by our algorithm.

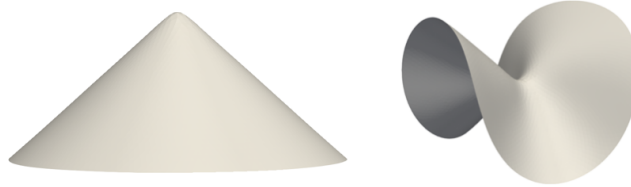


FIGURE 1. Computed solution with the blueprinted director field \mathbf{m}_1 that has degree 1 defect, $\lambda < 1$ and $\alpha_r = 0$ (right), $\pi/2$ (left). We refer to Section 5.1 for details of these numerical simulations.

Next, we introduce a solution induced by a director field with a degree 1/2 defect, which will help us construct an approximate solution for a degree 3/2 defect in Section 3.6. Motivated by [10], we consider the director field

$$(47) \quad \mathbf{m}_{1/2}(\mathbf{x}') = \begin{cases} \text{sign}(x_2)\mathbf{e}_2, & x_1 \geq 0 \\ \frac{\mathbf{x}'}{|\mathbf{x}'|}, & x_1 < 0, \end{cases}$$

and note that $\mathbf{m}_\perp \otimes \mathbf{m}_\perp$ is the typical line field for a defect of degree 1/2 at the origin. Since $\mathbf{m}_{1/2}(\mathbf{x}') = \mathbf{m}_1(\mathbf{x}')$ when $x_1 < 0$, we expect a cone configuration forming in the left half-plane. For $\lambda > 1$, an exact solution is given by the lifted surface configuration

$$(48) \quad \mathbf{y}_{1/2}(\mathbf{x}') = \left(\mathbf{x}'_\lambda, \phi_{1/2}(\mathbf{x}'_\lambda) \right)^T,$$

where

$$(49) \quad \phi_{1/2}(\mathbf{x}') = \begin{cases} \sqrt{\lambda^3 - 1} (1 - |x_2|), & x_1 \geq 0 \\ \sqrt{\lambda^3 - 1} (1 - |\mathbf{x}'|), & x_1 < 0 \end{cases}.$$

This entails stretching in the direction $\mathbf{m}_{1/2}$ and shrinking in the perpendicular direction $\mathbf{m}_{1/2}^\perp$, which in turn explains the shape of $\mathbf{y}_{1/2}$ in Fig. 2 for $x_1 > 0$. We see that when $x_1 < 0$, the map $\mathbf{y}_{1/2}$ coincides with the cone in (45). We plot $\mathbf{m}_{1/2}$ (left), $\mathbf{y}_{1/2}$ (middle) and our computed solution (right) in Fig.2.

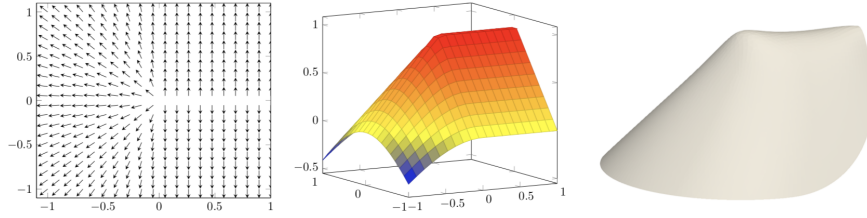


FIGURE 2. Director field $\mathbf{m}_{1/2}$ from (47) (left), lifted surface $\mathbf{y}_{1/2}$ from (48)-(49) for $\lambda = 2^{1/3}$ (middle), and computed solution in a unit disc domain with $\mathbf{m} = \mathbf{m}_{1/2}$ and a Dirichlet boundary condition that is compatible with (48)-(49) (right). Note that the gradient of $\phi_{1/2}$ is parallel to $\mathbf{m}_{1/2}$ whereas $\mathbf{m}_{1/2}^\perp$ is the typical director field for a $1/2$ defect.

3.3. Higher degree defects: main idea and idealized construction. We now consider rotationally symmetric blueprinted director fields \mathbf{m}_n with defects of integer degree $n > 1$. Such director fields are given in polar coordinates by

$$(50) \quad \mathbf{m}_n(r, \theta) = (\cos(n\theta), \sin(n\theta)).$$

We observe that the line field $\mathbf{m}_n \otimes \mathbf{m}_n$ in (40) exhibits a discontinuity at the origin. We denote by g_n the metric generated by \mathbf{m}_n and arbitrary λ via (36). Ideally, the goal is to build on the solution (45) for $n = 1$ and composition of defects to obtain a solution \mathbf{y}_n with degree n defect. The main idea is as follows.

We exploit the relation to the complex-valued function $f_n(z) = e^{in \arg(z)}$ to write

$$\mathbf{m}_n(\mathbf{x}') = p^{-1}(f_n(p(\mathbf{x}'))),$$

where $z = |z|e^{i \arg(z)}$ for any $z \in \mathbb{C}$ and $p : \mathbb{R}^2 \rightarrow \mathbb{C}$ is the map $p(\mathbf{x}') = x_1 + ix_2$. From this perspective, we can write a director field with degree n defect as the multiplication or composition of two director fields with degree 1 and $n - 1$ defects

$$e^{in \arg(z)} = e^{i \arg(z)} e^{i(n-1) \arg(z)}.$$

If $\mathbf{m}_1 := (\mu_1, \mu_2)$ and $\mathbf{m}_{n-1} := (\xi_1, \xi_2)$, then $\mu_1 + i\mu_2 = e^{i \arg(p(\mathbf{m}_1))}$ and $\xi_1 + i\xi_2 = e^{i \arg(p(\mathbf{m}_{n-1}))}$ imply

$$e^{i \arg(p(\mathbf{m}_n))} = (\mu_1 + i\mu_2)(\xi_1 + i\xi_2) = (\mu_1\xi_1 - \mu_2\xi_2) + i(\mu_1\xi_2 + \mu_2\xi_1).$$

Applying p^{-1} to both sides yields

$$(51) \quad \mathbf{m}_n = \begin{pmatrix} \mu_1 & -\mu_2 \\ \mu_2 & \mu_1 \end{pmatrix} \begin{pmatrix} \xi_1 \\ \xi_2 \end{pmatrix} = \mathbf{R}_1 \mathbf{m}_{n-1},$$

where $\mathbf{R}_1 := (\mathbf{m}_1, \mathbf{m}_1^\perp)$ is a rotation matrix that depends on \mathbf{x}' . In view of (40) we may write the metric g_n at \mathbf{x}' as

$$(52) \quad g_n = (\lambda^2 - \lambda^{-1}) \mathbf{R}_1 (\mathbf{m}_{n-1} \otimes \mathbf{m}_{n-1}) \mathbf{R}_1^T + \lambda^{-1} I_2.$$

Assuming $\lambda > 1$, we compare (52) with the metric that arises from function composition of two defects of degree 1 and $n-1$. With $\mathbf{x}'_\lambda = \lambda^{-1/2} \mathbf{x}'$ already defined in (42), we consider the following modified lifted surface

$$(53) \quad \mathbf{y}_n(\mathbf{x}') := \left(\mathbf{x}'_\lambda, \phi_n(\mathbf{v}(\mathbf{x}'_\lambda)) \right)^T.$$

Compared to either (45) or (48) of Section 3.1, we now compose ϕ_n with an unknown function $\mathbf{v} : \lambda^{-1/2} \Omega \rightarrow \lambda^{-1/2} \Omega$. We then apply the chain rule to determine

$$(54) \quad \mathbb{I}[\mathbf{y}_n(\mathbf{x}')] = \lambda^{-1} I_2 + \lambda^{-1} \nabla \mathbf{v}(\mathbf{x}'_\lambda)^T (\nabla \phi_n(\mathbf{v}(\mathbf{x}'_\lambda)) \otimes \nabla \phi_n(\mathbf{v}(\mathbf{x}'_\lambda))) \nabla \mathbf{v}(\mathbf{x}'_\lambda).$$

To match (52) an ideal construction would be to find ϕ_n and \mathbf{v} so that $\nabla \phi_n(\mathbf{v}(\mathbf{x}'_\lambda)) = \sqrt{\lambda^3 - 1} \mathbf{m}_{n-1}(\mathbf{x}')$ and $\nabla \mathbf{v}(\mathbf{x}'_\lambda) = \mathbf{R}_1(\mathbf{x}')^T$. We will find ϕ_n in terms of ϕ_{n-1} , but before we do so we need to argue with \mathbf{v} . An ideal \mathbf{v} should have a gradient whose rows are \mathbf{m}_1 and \mathbf{m}_1^\perp . Since \mathbf{m}_1 points radially outward and \mathbf{m}_1^\perp is tangent to concentric circles, the choice of \mathbf{v} in polar coordinates should be $\mathbf{v}(r, \theta) = (v_1(r), v_2(\theta))$ in order for the rows of $\nabla \mathbf{v}$ to be parallel to \mathbf{m}_1 and \mathbf{m}_1^\perp . One such choice of \mathbf{v} is

$$(55) \quad \mathbf{v}(r, \theta) = \begin{pmatrix} a \log r \\ a \theta \end{pmatrix}$$

for $a > 0$, whose gradient in Euclidean coordinates is formally

$$(56) \quad \nabla \mathbf{v}(\mathbf{x}') = \frac{a}{|\mathbf{x}'|} \mathbf{R}_1(\mathbf{x}')^T.$$

The choice of $v_1(r) = a \log r$ is so that the scaling of $\frac{1}{r}$ matches the gradient of $v_2(\theta) = a\theta$. Here, $\nabla \mathbf{v}$ matches $\mathbf{R}_1(\mathbf{x})^T$ up to the scaling $\frac{a}{|\mathbf{x}'|}$, and we nearly recover the ideal \mathbf{v} . Finding a vector field \mathbf{v} whose gradient equals a space-dependent rotation $\mathbf{R}_1(\mathbf{x}')^T$ is questionable. In fact, in order for $\text{curl}(\psi(r) \mathbf{m}_1^\perp(\mathbf{x})) = 0$ and potentially have an antiderivative, the only choice of ψ is $\psi(r) = \frac{a}{r}$. Therefore, $\psi(|\mathbf{x}'|) = \frac{a}{|\mathbf{x}'|}$ is the only scaling for which one may hope to find an antiderivative of $\psi(|\mathbf{x}'|) \mathbf{R}_1(\mathbf{x}')^T$. The choice of ϕ_n is designed to compensate for this scaling. If

$$(57) \quad \phi_n(\mathbf{x}') := \frac{\sqrt{\lambda^3 - 1}}{n a^{n-1}} |\mathbf{x}'|^n \quad \Rightarrow \quad \nabla \phi_n(\mathbf{x}') = \frac{|\mathbf{x}'|}{a} \nabla \phi_{n-1}(\mathbf{x}'),$$

which is consistent with (46) for $n = 1$. Combining the inductive hypothesis

$$\nabla \phi_{n-1}(\mathbf{v}(\mathbf{x}'_\lambda)) = \sqrt{\lambda^3 - 1} \mathbf{m}_{n-1}(\mathbf{x}'),$$

with the recursion relation (57) yields

$$\begin{aligned} \nabla [\phi_n(\mathbf{v}(\mathbf{x}'_\lambda))] &= \nabla \mathbf{v}(\mathbf{x}'_\lambda)^T \nabla \phi_n(\mathbf{v}(\mathbf{x}'_\lambda)) = \frac{|\mathbf{v}(\mathbf{x}'_\lambda)|}{|\mathbf{x}'_\lambda|} \mathbf{R}_1(\mathbf{x}'_\lambda) \nabla \phi_{n-1}(\mathbf{v}(\mathbf{x}'_\lambda)) \\ &= \frac{|\mathbf{v}(\mathbf{x}'_\lambda)|}{|\mathbf{x}'_\lambda|} \sqrt{\lambda^3 - 1} \mathbf{R}_1(\mathbf{x}') \mathbf{m}_{n-1}(\mathbf{x}') = \frac{|\mathbf{v}(\mathbf{x}'_\lambda)|}{|\mathbf{x}'_\lambda|} \sqrt{\lambda^3 - 1} \mathbf{m}_n(\mathbf{x}'). \end{aligned}$$

This shows that we need $|\mathbf{v}(\mathbf{x}')| = |\mathbf{x}'|$ to close the argument, which may not be possible unless $\mathbf{v}(\mathbf{x}') = \mathbf{R}(\mathbf{x}')^T \mathbf{x}'$ with $\mathbf{R}(\mathbf{x}')$ a rotation. This in turn would not lead to (56). Finally, the cone solution for $n = 1$ satisfies $\nabla \phi_1(\mathbf{x}'_\lambda) = \pm \sqrt{\lambda^3 - 1} \mathbf{m}_1(\mathbf{x}')$, whereas the ideal construction requires $\nabla \phi_1(\mathbf{v}(\mathbf{x}'_\lambda)) = \pm \sqrt{\lambda^3 - 1} \mathbf{m}_1(\mathbf{x}')$. The sign does not matter because g_1 is invariant under $\mathbf{m}_1 \mapsto -\mathbf{m}_1$, but there is a mismatch in the argument of $\nabla \phi_1$ since $\mathbf{v}(\mathbf{x}'_\lambda)$ may not be equal to \mathbf{x}'_λ everywhere. We next discuss how to circumvent these obstructions to the idealized construction via approximation.

3.4. Formal approximation of idealized construction. We now build an approximate deformation \mathbf{y}_n such that $\mathbf{I}[\mathbf{y}_n] \approx g_n$. To this end, we modify \mathbf{v} from (55), so that $\mathbf{v}(\mathbf{x}'_\lambda) \approx \mathbf{x}'_\lambda$ near the point $\mathbf{x}^* = (a, 0)^T$ for $a > 0$; this avoids a singularity at $\mathbf{0}$. To guarantee that $\mathbf{v}(\mathbf{x}^*) = \mathbf{x}^*$ and $\nabla \mathbf{v}(\mathbf{x}^*) = I_2$, we choose

$$(58) \quad \mathbf{v}(\mathbf{x}') = \begin{pmatrix} \frac{a}{2} \log(x_1^2 + x_2^2) + C_a \\ a \arctan(x_2/x_1) \end{pmatrix},$$

where $C_a = a - a \log(a)$. Hence, \mathbf{v} satisfies (56) and the formal Taylor expansion

$$\mathbf{v}(\mathbf{x}') = \mathbf{x}^* + (\mathbf{x}' - \mathbf{x}^*) + \mathcal{O}(|\mathbf{x}' - \mathbf{x}^*|^2) = \mathbf{x}' + \mathcal{O}(|\mathbf{x}' - \mathbf{x}^*|^2),$$

or equivalently the following expression in the rescaled coordinates \mathbf{x}'_λ

$$(59) \quad \mathbf{v}(\mathbf{x}'_\lambda) = \mathbf{x}'_\lambda + \mathcal{O}(|\mathbf{x}' - \mathbf{x}^*|^2),$$

because $\lambda = \mathcal{O}(1)$. Using (59), we approximately satisfy the three crucial requirements

$$\begin{aligned} |\mathbf{v}(\mathbf{x}'_\lambda)|^2 &= |\mathbf{x}'_\lambda|^2 + \mathcal{O}(|\mathbf{x}' - \mathbf{x}^*|^2), \\ \mathbf{m}_1(\mathbf{v}(\mathbf{x}'_\lambda)) &= \mathbf{m}_1(\mathbf{x}'_\lambda) + \mathcal{O}(|\mathbf{x}' - \mathbf{x}^*|^2), \\ \nabla[\phi_n(\mathbf{v}(\mathbf{x}'_\lambda))] &= \sqrt{\lambda^3 - 1} \mathbf{m}_n(\mathbf{x}') + \mathcal{O}(|\mathbf{x}' - \mathbf{x}^*|^2). \end{aligned}$$

Inserting these formal approximations into (54) yields a map \mathbf{y}_n defined by (53) for $n \geq 2$ that approximately satisfies the metric constraint in a vicinity of \mathbf{x}^*

$$(60) \quad \mathbf{I}[\mathbf{y}_n(\mathbf{x}')] = g_n(\mathbf{x}') + \mathcal{O}(|\mathbf{x}' - \mathbf{x}^*|^2).$$

3.5. Approximate surfaces for defects of degree two. We now specialize the above construction for $n = 2$. In view of (57), we realize that

$$\phi_2(\mathbf{x}') := \frac{\sqrt{\lambda^3 - 1}}{2a} |\mathbf{x}'|^2 \quad \Rightarrow \quad \nabla \phi_2(\mathbf{x}') = \frac{\sqrt{\lambda^3 - 1}}{a} \mathbf{x}' = \frac{\sqrt{\lambda^3 - 1}}{a} |\mathbf{x}'| \mathbf{m}_1(\mathbf{x}'),$$

Hence, (53) gives an approximate map \mathbf{y}_2 with

$$\phi_2(\mathbf{v}(\mathbf{x}')) = \frac{\sqrt{\lambda^3 - 1}}{2a} \left(\left(\frac{a}{2} \log(x_1^2 + x_2^2) + a - a \log a \right)^2 + a^2 \arctan^2\left(\frac{x_2}{x_1}\right) \right),$$

for $x_1 > 0$ and any $a > 0$ not be too large so that \mathbf{y}_2 captures the correct defect configuration. We display $\phi \circ \mathbf{v}$ for $a = .75, \lambda = 1.1$ in Fig. 3, reflected for $x_1 < 1$ to account for symmetry, along with the computed solution from Section 5.1.

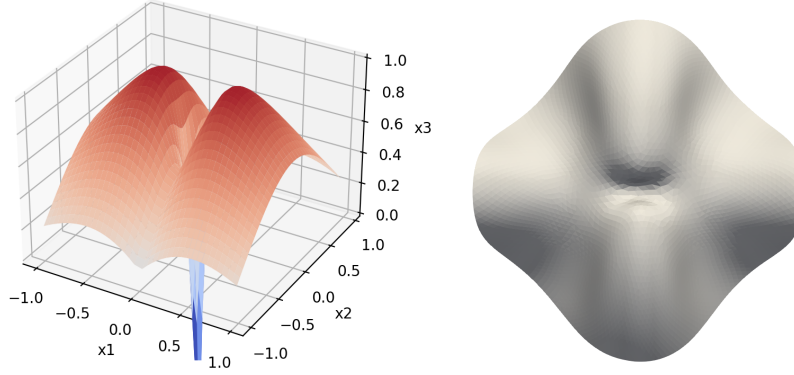


FIGURE 3. Approximate lifted surface for degree 2 defect (left) and computed solution with the director field \mathbf{m}_2 in Section 5.1 (right). Our derivation requires $x_1 > 0$, but the solution should be symmetric across the x_2x_3 plane, which is why we plot a reflected solution for $x_1 < 0$. We recover two bumps, consistent with the simulation but at the cost of a singularity at the origin.

3.6. Approximate surface for degree 3/2 defect. We now apply the above approach of composing defects, but for a defect of degree 3/2. We intend to explain the intriguing “bird beak” shape observed in our computations displayed in Figures 4 and 5. We first observe that the explicit expressions (48) and (49) for a defect of degree 1/2 do not quite conform with (50) for $n = 1/2$, except in the vicinity of the origin. Motivated by the recursion relation (51), we still write the degree 3/2 director field as

$$(61) \quad \mathbf{m}_{3/2}(\mathbf{x}') = \mathbf{R}_1(\mathbf{x}') \mathbf{m}_{1/2}(\mathbf{x}'),$$

with $\mathbf{m}_{1/2}$ given in (47). We now construct an approximate map $\mathbf{y}_{3/2}$ such that

$$\mathbb{I}[\mathbf{y}_{3/2}(\mathbf{x}')] \approx g_{3/2}(\mathbf{x}') = (\lambda^2 - \lambda^{-1}) \mathbf{m}_{3/2}(\mathbf{x}') \otimes \mathbf{m}_{3/2}(\mathbf{x}') + \lambda^{-1} I_2,$$

according to (52) for $\lambda > 1$. The deformation $\mathbf{y}_{3/2}$ satisfies in turn (53), namely

$$(62) \quad \mathbf{y}_{3/2}(\mathbf{x}') = (\mathbf{x}'_\lambda, \phi_{3/2}(\mathbf{v}(\mathbf{x}'_\lambda)))^T$$

with $\phi_{3/2}$ related to $\phi_{1/2}$ via (57). Since we are interested in an approximation for $x_1 > 0$ to capture the “bird beak” structure, we deduce from (49)

$$\nabla \phi_{3/2}(\mathbf{x}') = \frac{|\mathbf{x}'|}{a} \nabla \phi_{1/2}(\mathbf{x}') \quad \Rightarrow \quad \nabla \phi_{3/2}(\mathbf{x}') = \sqrt{\lambda^3 - 1} \frac{|\mathbf{x}'|}{a} \text{sign}(x_2) \mathbf{e}_2.$$

Unfortunately, this ideal relation is incompatible because $\text{curl}(\frac{|\mathbf{x}'|}{a} \text{sign}(x_2) \mathbf{e}_2) \neq 0$ and we need to amend the construction of $\phi_{3/2}$ by approximation. To this end, we define for $x_1 > 0$ the following modification of $\phi_{3/2}$

$$(63) \quad \phi_{3/2}(\mathbf{x}') = \sqrt{\lambda^3 - 1} \left(1 - \frac{1}{a} \int_0^{|x_2|} \sqrt{s^2 + x_1^2} ds \right),$$

whose gradient is

$$\nabla \phi_{3/2}(\mathbf{x}') = -\sqrt{\lambda^3 - 1} \frac{|\mathbf{x}'|}{a} \text{sign}(x_2) \mathbf{e}_2 - \sqrt{\lambda^3 - 1} \frac{1}{a} \left(\int_0^{|x_2|} \frac{x_1}{\sqrt{s^2 + x_1^2}} ds \right) \mathbf{e}_1.$$

Exploiting that the integrand in the second term is bounded by 1 yields

$$\nabla \phi_{3/2}(\mathbf{x}) = -\sqrt{\lambda^3 - 1} \frac{|\mathbf{x}|}{a} \text{sign}(x_2) \mathbf{e}_2 - \frac{\sqrt{\lambda^3 - 1}}{a} \mathcal{O}(|x_2|).$$

To approximate the first fundamental form $\mathbb{I}[\mathbf{y}_{3/2}]$, we recall (54) and compute

$$\nabla \mathbf{v}(\mathbf{x}'_\lambda)^T \nabla \phi(\mathbf{v}(\mathbf{x}'_\lambda)) = \sqrt{\lambda^3 - 1} \mathbf{R}_1(\mathbf{x}'_\lambda) \frac{|\mathbf{v}(\mathbf{x}'_\lambda)|}{|\mathbf{x}'_\lambda|} \text{sign}(\mathbf{v}(\mathbf{x}'_\lambda)_2) \mathbf{e}_2 + \mathcal{O}(|\mathbf{v}(\mathbf{x}'_\lambda)_2|),$$

where $\mathbf{v}(\mathbf{x}'_\lambda)_2 = a \arctan(x_2/x_1)$ denotes the second component of $\mathbf{v}(\mathbf{x}'_\lambda)$ written in (58). We thus deduce $\text{sign}(\mathbf{v}(\mathbf{x}'_\lambda)_2) = \text{sign}(x_2)$ for $x_1 > 0$ and, employing that $\mathbf{m}_{1/2}(\mathbf{x}) = \text{sign}(x_2) \mathbf{e}_2$ for $x_1 > 1$ along with (61), we arrive at

$$\nabla \mathbf{v}(\mathbf{x}'_\lambda)^T \nabla \phi(\mathbf{v}(\mathbf{x}'_\lambda)) = \sqrt{\lambda^3 - 1} \mathbf{m}_{3/2}(\mathbf{x}') + \mathcal{O}(|x_2|) + \mathcal{O}(|\mathbf{x}' - \mathbf{x}^*|^2),$$

because $\arctan(x_2/x_1) = \mathcal{O}(|x_2|)$ for x_1 away from 0. The expression (62) for $\mathbf{y}_{3/2}$ with $\phi_{3/2}$ defined in (63) gives an approximate shape profile that satisfies

$$\mathbb{I}[\mathbf{y}_{3/2}(\mathbf{x}')] = g_{3/2}(\mathbf{x}') + \mathcal{O}(|x_2|) + \mathcal{O}(|\mathbf{x} - \mathbf{x}^*|^2).$$

The contour plot of the corresponding lifted surface $\phi_{3/2}(\mathbf{v}(\mathbf{x}'_\lambda))$ is displayed in Fig. 4 (left) for $a = .75$. We note that the profile has a similar bird beak shape to the computational result reported in Fig. 4 (right) and Fig. 5. For the $x_1 < 0$, $\mathbf{m}_{1/2}(\mathbf{x}') = \mathbf{m}_1(\mathbf{x}')$, and one can apply the arguments in Section 3.5 to get the asymptotic profile for $x_1 < 0$.

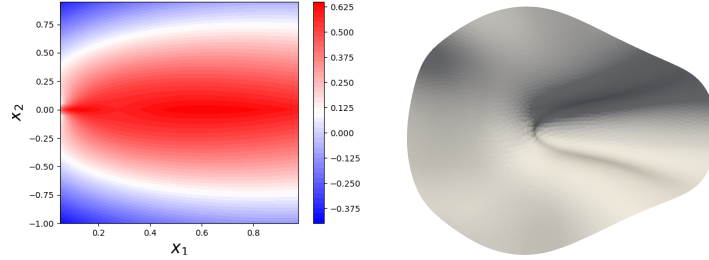


FIGURE 4. Contour plot of approximate lifted surface for degree 3/2 defect for $a = .75$ and $x_1 > 0$ (left) and computational result for a degree 3/2 defect obtained in Section 5.1. The profile matches the computed “bird beak” shape. To see this, notice that contour lines pinch off as $x_1 \rightarrow 0$. As a result, the lifted surface gets steeper near the origin. This helps explain the “bird beak” shape.

The compositional method explains why we should expect the intriguing “bird beak”. We now provide a heuristic explanation. If a is fixed but x_1 is small, we drop x_1 in the integrand of (63), and $\phi_{3/2}(\mathbf{x}')$ behaves like $\tilde{\phi}_{3/2}(\mathbf{x}') := \sqrt{\lambda^3 - 1} \left(1 - \frac{1}{2a} |x_2|^2\right)$. We see that level sets of this function are straight lines $|x_2| = \text{constant}$ that increase as $|x_2|$ decreases to 0, very much like level sets of $\phi_{1/2}(\mathbf{x}')$ in (49) for $x_1 > 0$. On the other hand, the lifted surface $\phi_{3/2}(\mathbf{v}(\mathbf{x}'_\lambda))$ from (62) behaves like

$$(64) \quad \tilde{\phi}_{3/2}(\mathbf{v}(\mathbf{x}'_\lambda)) = \sqrt{\lambda^3 - 1} \left(1 - \frac{a}{2} \arctan\left(\frac{|x_2|}{x_1}\right)^2\right),$$

whose level sets are radial lines $\frac{|x_2|}{x_1} = \text{constant}$ that increase as $\frac{|x_2|}{x_1}$ decreases to 0. Therefore, the lifted surface $\tilde{\phi}_{3/2}(\mathbf{v}(\mathbf{x}'_\lambda))$ pinches off at the origin in the sense that it develops a discontinuity. In Section 3.3 we advocated that a defect of degree 3/2 could be viewed as a composition of degree 1/2 and 1 defects. The effect of the degree 1 defect on (48) is to twist or compress the horizontal level sets of $\phi_{1/2}(\mathbf{v}(\mathbf{x}'_\lambda))$ into radial level sets of $\tilde{\phi}_{3/2}(\mathbf{v}(\mathbf{x}'_\lambda))$. This is due to the action of the vector-valued map \mathbf{v} and boils down to the replacement of $|x_2|$ in (49) by $\frac{a}{2} \arctan\left(\frac{|x_2|}{x_1}\right)^2$ in (64).

4. FINITE ELEMENT METHOD WITH REGULARIZATION

In this section, we introduce a finite element discretization to (9) and an iterative scheme to solve the consequent nonlinear discrete problem.

4.1. Discretization. We consider a shape-regular family $\{\mathcal{T}_h\}$ of simplicial meshes of Ω parametrized by the mesh size $h = \max_{T \in \mathcal{T}_h} h_T$, where $h_T = \text{diam}(T)$. We denote by \mathcal{N}_h the set of vertices of \mathcal{T}_h , and by \mathcal{E}_h the set of interior edges of \mathcal{T}_h .

For any $T \in \mathcal{T}_h$, we denote by $\mathcal{P}_1(T)$ the space of first-degree polynomials on T and by $\mathcal{N}_h(T)$ the set of vertices of T . We consider the space of \mathcal{T}_h -piecewise affine and globally continuous functions

$$\mathbb{V}_h := \left\{ \mathbf{v}_h \in C^0(\bar{\Omega}; \mathbb{R}^3) : \mathbf{v}_h|_T \in [\mathcal{P}_1(T)]^3 \text{ for all } T \in \mathcal{T}_h \right\},$$

and note that $\mathbb{V}_h \subset H^1(\Omega; \mathbb{R}^3)$. We write \mathbb{V}_h^* to designate the dual space of \mathbb{V}_h and denote by I_h the nodal Lagrange interpolation operator $I_h : C^0(\bar{\Omega}; \mathbb{R}^3) \rightarrow \mathbb{V}_h$.

We now introduce the jump operators. To this end, let \mathbf{n}_e be a unit normal to $e \in \mathcal{E}_h$ (the orientation is chosen arbitrarily but is fixed once for all). Given a scalar piecewise polynomial function v_h over \mathcal{T}_h and $e \in \mathcal{E}_h$, we set

$$(65) \quad [v_h]_e := v_h^- - v_h^+,$$

where $v_h^\pm(\mathbf{x}') := \lim_{s \rightarrow 0^\pm} v_h(\mathbf{x}' \pm s\mathbf{n}_e)$ for $\mathbf{x}' \in e$; jumps of vector-valued and tensor-valued functions are computed component-wise. Note that for $\mathbf{v}_h \in \mathbb{V}_h$, we have $[\mathbf{v}_h]_e = 0$ for any $e \in \mathcal{E}_h$, while $[\nabla \mathbf{v}_h]_e \neq 0$ in general.

We propose the discrete energy $E_h : \mathbb{V}_h \rightarrow \mathbb{R}$ to be

$$(66) \quad E_h[\mathbf{y}_h] = E_{str}[\mathbf{y}_h] + R_h[\mathbf{y}_h],$$

where the first term is the stretching energy defined in (9) and (10), while R_h is a regularization term defined in (16) and recall now

$$(67) \quad R_h[\mathbf{y}_h] := \sum_{e \in \mathcal{E}_h} \int_e c_r h_e [\nabla \mathbf{y}_h]^2,$$

where $c_r : \mathcal{E}_h \rightarrow \mathbb{R}$ is a non-negative regularization parameter that may vanish on some edges to allow for folding. This is a crucial computational feature of the discrete counterpart of (9), which reads

$$(68) \quad \mathbf{y}_h^* \in \operatorname{argmin}_{\mathbf{y}_h \in \mathbb{V}_h} E_h[\mathbf{y}_h].$$

4.2. Regularization. This section is dedicated to a discussion of the regularization term R_h . We add R_h to deal with the non-convexity of the stretching energy density W_{str} given in (10). We refer to our accompanying paper [45] for a detailed discussion of the lack-of-convexity and other possible strategies to treat it. We also prove in [45] convergence of discrete minimizers of (68).

We first point out that, in the discontinuous Galerkin (DG) contexts (for instance [48, 49]), a discrete H^2 semi-norm is defined as

$$(69) \quad |\mathbf{y}_h|_{H_h^2(\Omega)}^2 := \|D_h^2 \mathbf{y}_h\|_{L^2(\Omega)}^2 + \sum_{e \in \mathcal{E}_h} h_e^{-1} \|[\nabla \mathbf{y}_h]\|_{L^2(e)}^2 + \sum_{e \in \mathcal{E}_h} h_e^{-3} \|[\mathbf{y}_h]\|_{L^2(e)}^2,$$

where D_h^2 denotes a piecewise Hessian on every element. Substituting continuous piecewise affine $\mathbf{y}_h \in \mathbb{V}_h$ into (69), we can see that only the second term remains while other terms vanish. This motivates our choice (67) for the regularization term (67), which in fact further satisfies $R_h[\mathbf{y}_h] \approx h^2 |\mathbf{y}_h|_{H_h^2(\Omega)}^2$ provided c_r is uniformly positive and \mathcal{T}_h is quasi-uniform. We note that $|\mathbf{y}_h|_{H_h^2(\Omega)}^2$ scales oscillations of the elementwise constant $\nabla \mathbf{y}_h$ between adjacent elements of \mathcal{T}_h for $\mathbf{y}_h \in \mathbb{V}_h$ and, consequently, can be viewed as a discrete approximation of the *Hessian* of \mathbf{y}_h .

We emphasize that a full model of LCNs is a blending of stretching energy and bending energy, which comes from higher order terms in the thickness t in the expansion (19) [16, 23, 25, 24]. This leads to a bending energy that incorporates the second fundamental form $\Pi[\mathbf{y}]$, and thus to a nonlinear combination of second order derivatives of the deformations \mathbf{y} . Ideally, one is able to express this energy in terms of the Hessian of \mathbf{y} [50, 51, 52, 49]. In the context of piecewise affine deformations $\mathbf{y}_h \in \mathbb{V}_h$, second order derivative information is contained in $|\mathbf{y}_h|_{H_h^2(\Omega)}$ and so in $R_h[\mathbf{y}_h]$. Therefore, for c_r uniformly positive and \mathcal{T}_h quasi-uniform, one can compare $R_h[\mathbf{y}_h] \approx h^2 |\mathbf{y}_h|_{H_h^2(\Omega)}^2$ with the scaled bending energy $t^2 E_{ben}[\mathbf{y}] := t^2 \|D^2 \mathbf{y}\|_{L^2(\Omega)}^2$, and realize that the meshsize parameter h plays a similar role to the thickness parameter t in the expansion of $\frac{1}{t} E_{3D}$ using (19) [16, 23, 25, 24]. Moreover, allowing c_r to vanish over a polygonal Γ made of edges of \mathcal{E}_h mimics discretely a material amenable to folding across Γ [53, 54]. We prove convergence of minimizers of (68) with folding in our companion paper [45]. The statement reads as follows.

Theorem 1 (convergence of discrete minimizers). *Let $\Omega \setminus \Gamma = \cup_{i=1}^I \Omega_i$ be a decomposition of Ω into disjoint subdomains Ω_i due to the creases Γ . Let the target metric g in (36) admit an isometric immersion $\mathbf{y} \in W^{1,\infty}(\Omega; \mathbb{R}^3)$, i.e. $\mathbb{I}[\mathbf{y}] = g$ a.e. in Ω , that satisfies $\mathbf{y}|_{\Omega_i} \in H^2(\Omega_i; \mathbb{R}^3) \cap C^1(\overline{\Omega}_i; \mathbb{R}^3)$ for all $i = 1, \dots, I$. Then there is a constant $\Lambda > 0$ such that discrete minimizers \mathbf{y}_h^* of (68) satisfy the energy scaling*

$$(70) \quad E_h[\mathbf{y}_h^*] \leq \Lambda h^2.$$

In addition, if a minimizer \mathbf{y}_h^ satisfies (70) and $\bar{\mathbf{y}}_h^* := |\Omega|^{-1} \int_{\Omega} \mathbf{y}_h^*$ is its meanvalue, then there exists a subsequence (not relabeled) such that $\mathbf{y}_h^* - \bar{\mathbf{y}}_h^* \rightarrow \mathbf{y}^*$ converges strongly in $H^1(\Omega; \mathbb{R}^3)$ to a function $\mathbf{y}^* \in W^{1,\infty}(\Omega; \mathbb{R}^3) \cap H^2(\Omega \setminus \Gamma; \mathbb{R}^3)$ that satisfies $E_{str,\Gamma}[\mathbf{y}^*] = \int_{\Omega \setminus \Gamma} W_{str}(\mathbf{x}', \nabla \mathbf{y}^*) d\mathbf{x}' = 0$ and $\mathbb{I}[\mathbf{y}^*] = g$ a.e. in Ω .*

We regard (67) as a discrete regularization mechanism rather than a discrete form of the bending energy $E_{ben}[\mathbf{y}]$, even though such a simplified form of $E_{ben}[\mathbf{y}]$ has been considered widely in the literature; we refer for instance [26, 23]. The true bending energy [16, 23, 25] involves $\Pi[\mathbf{y}]$ and its reduction to $D^2 \mathbf{y}$ is a matter of current research. We leave this topic for a future study.

Moreover, we view (67) as a mechanism for equilibria selection. In the absence of regularization, i.e. $c_r = 0$ in (67), minimizers $\mathbf{y}_h^* \in \mathbb{V}_h$ of (68) can exhibit extra bumps and wrinkling which have negligible influence on the stretching energy. This is a manifestation of lack of convexity of W_{str} , and thus of uniqueness, and leads to the formation of micro-structure [50]. This topic is well studied in the theory and computation of nonlinear elasticity, but it is not the focus of this paper. We invoke (67) to suppress numerical oscillations in Section 5.5 as well as to allow for folding in the development of compatible origami-structures in Section 5.2 and incompatible origami-structures in Section 5.3. The latter lead to weak limits $y^* \in H^1(\Omega; \mathbb{R}^3)$ with $E_{str}[\mathbf{y}^*] > 0$, so they are not minimizers of the stretching energy E_{str} .

4.3. Iterative solver. We design a nonlinear discrete gradient flow to find a solution to (68) in this subsection. Due to the stretching energy being non-quadratic and non-convex, we end up with a nonlinear non-convex discrete problem to solve.

4.3.1. Nonlinear gradient flow. Implicit gradient flows are robust methods to find stationary points of energy functionals E regardless of their convexity, and have the advantage of built-in energy stability; they belong to the class of energy descent methods. Consider the auxiliary evolution equation $\partial_t A[\mathbf{y}] + \delta E[\mathbf{y}] = 0$, where A is a symmetric elliptic operator, $\delta E[\mathbf{y}]$ stands for the first variation of E , and t is a pseudo-time. The backward Euler discretization reads: given \mathbf{y}^n solve for \mathbf{y}^{n+1}

$$\frac{1}{\tau} (A\mathbf{y}^{n+1} - A\mathbf{y}^n) + \delta E[\mathbf{y}^{n+1}] = 0,$$

where τ is the time-step discretization parameter. The weak formulation of this semi-discrete equation is equivalent to minimizing the augmented functional

$$(71) \quad L^n[\mathbf{y}] := \frac{1}{2\tau} \|\mathbf{y} - \mathbf{y}^n\|_A^2 + E[\mathbf{y}]$$

where $\|\cdot\|_A$ is the norm associated with the operator A , i.e. $\|\mathbf{y}\|_A^2 := \langle A\mathbf{y}, \mathbf{y} \rangle$. This can be reinterpreted as finding a minimizer of E constrained to be closed to \mathbf{y}^n ; so the first term in (71) penalizes the deviation of \mathbf{y} from \mathbf{y}^n in the A -norm.

Since the stretching energy E_{str} from (9) and (10) is formulated in $H^1(\Omega; \mathbb{R}^3)$, we choose $A = I - \Delta$ and the corresponding norm to be the $H^1(\Omega)$ -norm. This choice has the property of making L^n convex in $H^1(\Omega; \mathbb{R}^3)$ provided \mathbf{y}^n is sufficiently smooth. With this in mind, we devise a discrete counterpart of (71) to find stationary points of E_h in (66) and, under some additional assumptions on the current iterate $\mathbf{y}_h^n \in \mathbb{V}_h$ to be discussed below, solve (67). We thus minimize

$$(72) \quad L_h^n[\mathbf{y}_h] := \frac{1}{2\tau} \|\mathbf{y}_h - \mathbf{y}_h^n\|_{H^1(\Omega)}^2 + E_h[\mathbf{y}_h],$$

whose Euler-Lagrange equation results from computing the first order variation of $L_h^n[\mathbf{y}_h]$ in the direction \mathbf{v}_h

$$(73) \quad \delta L_h^n[\mathbf{y}_h](\mathbf{v}_h) = \frac{1}{\tau} (\mathbf{y}_h, \mathbf{v}_h)_{H^1(\Omega)} + \delta E_h[\mathbf{y}_h](\mathbf{v}_h) - F_h^n(\mathbf{v}_h) = 0 \quad \forall \mathbf{v}_h \in \mathbb{V}_h,$$

where $F_h^n \in \mathbb{V}_h^*$ is defined as

$$F_h^n(\mathbf{v}_h) := \frac{1}{\tau} (\mathbf{y}_h^n, \mathbf{v}_h)_{H^1(\Omega)},$$

and

$$\delta E_h[\mathbf{y}_h](\mathbf{v}_h) = \delta E_{str}[\mathbf{y}_h](\mathbf{v}_h) + \delta R_h[\mathbf{y}_h](\mathbf{v}_h).$$

A direct but tedious computation shown in Appendix A gives an explicit expression for $\delta E_{str}[\mathbf{y}_h](\mathbf{v}_h)$, which turns out to depend *nonlinearly* on \mathbf{y}_h . Therefore, (73) is a nonlinear discrete equation for $\mathbf{y}_h \in \mathbb{V}_h$.

We now state the energy stability of (72) provided (73) is solved exactly. This is a natural property for *implicit* gradient flows.

Theorem 2 (energy stability). *Given $\mathbf{y}_h^n \in \mathbb{V}_h$ for any $n \geq 0$, suppose $\mathbf{y}_h^{n+1} \in \mathbb{V}_h$ minimizes $L_h^n[\mathbf{y}_h]$ defined in (72). Then $E_h[\mathbf{y}_h^{n+1}] \leq E_h[\mathbf{y}_h^n]$, and the inequality is strict if $\mathbf{y}_h^{n+1} \neq \mathbf{y}_h^n$. Moreover, for any $N \geq 1$,*

$$(74) \quad E_h[\mathbf{y}_h^N] + \frac{1}{2\tau} \sum_{n=0}^{N-1} \|\mathbf{y}_h^{n+1} - \mathbf{y}_h^n\|_{H^1(\Omega)}^2 \leq E_h[\mathbf{y}_h^0].$$

Proof. Since \mathbf{y}_h^{n+1} minimizes L_h^n , we have $L_h^n[\mathbf{y}_h^{n+1}] \leq L_h^n[\mathbf{y}_h^n]$, whence

$$\frac{1}{2\tau} \|\mathbf{y}_h^{n+1} - \mathbf{y}_h^n\|_{H^1(\Omega)}^2 + E_h[\mathbf{y}_h^{n+1}] = L_h^n[\mathbf{y}_h^{n+1}] \leq L_h^n[\mathbf{y}_h^n] = E_h[\mathbf{y}_h^n].$$

This proves monotonicity of $E_h[\mathbf{y}_h^n]$ and, adding over $n = 1 : N-1$, yields (74). \square

Moreover, given a tolerance $\text{tol}_1 > 0$, we stop the nonlinear gradient flow when

$$\frac{1}{\tau} |E_h[\mathbf{y}_h^N] - E_h[\mathbf{y}_h^{N-1}]| < \text{tol}_1$$

is satisfied for some $N > 0$. The function $\mathbf{y}_h^N \in \mathbb{V}_h$ is the desired output. We next discuss how we solve the nonlinear equation (73).

4.3.2. Newton sub-iteration. We solve each step n of the iterative scheme (73) by a Newton-type sub-iteration. In fact, we let $\mathbf{y}_h^{n,0} := \mathbf{y}_h^n$ and assume $\mathbf{y}_h^{n,k} \in \mathbb{V}_h$ is given. We then solve for the increment $\delta \mathbf{y}_h^{n,k} \in \mathbb{V}_h$ by

$$(75) \quad \delta^2 L_h^n[\mathbf{y}_h^{n,k}](\delta \mathbf{y}_h^{n,k}, \mathbf{v}_h) = -\delta L_h^n[\mathbf{y}_h^{n,k}](\mathbf{v}_h) \quad \forall \mathbf{v}_h \in \mathbb{V}_h,$$

and update $\mathbf{y}_h^{n,k+1} := \mathbf{y}_h^{n,k} + \delta \mathbf{y}_h^{n,k}$. Equation (75) is *linear* in the unknown $\delta \mathbf{y}_h^{n,k}$ because $\mathbf{y}_h^{n,k}$ is known. Moreover, given a tolerance tol_2 , we stop (75) when

$$|\delta L_h^n[\mathbf{y}_h^{n,M}](\delta \mathbf{y}_h^{n,M})|^{1/2} \leq \text{tol}_2,$$

for some integer $M > 0$ and set $\mathbf{y}_h^{n+1} := \mathbf{y}_h^{n,M}$. The expression of $\delta^2 L_h^n[\mathbf{y}_h](\mathbf{v}_h, \mathbf{w}_h)$ for $\mathbf{y}_h, \mathbf{v}_h, \mathbf{w}_h \in \mathbb{V}_h$ is tedious to compute but is given in Appendix A.

The next natural question is whether the Newton equation (75) is well-posed in each sub-step n and $\mathbf{y}_h^{n,k}$ converges to a minimizer of (72) as $k \rightarrow \infty$ in a neighborhood of the previous iterate \mathbf{y}_h^n , provided τ is sufficiently small. Heuristically, the lack of convexity of the stretching energy works against the well-posedness and convergence of the Newton sub-iteration, but the flow metric $\tau^{-1}(\cdot, \cdot)_{H^1(\Omega)}$ in (73) is chosen to dominate $\delta E_h[\mathbf{y}_h^n]$ when τ is small enough.

We now discuss properties of the proposed Newton sub-iteration (75). We first state the following ellipticity of $\delta^2 L_h^n[\mathbf{y}_h](\cdot, \cdot)$ but prove it in Appendix A.

Theorem 3 (ellipticity). *Given $\mathbf{y}_h \in \mathbb{V}_h$, let the piecewise constant eigenvalues $\lambda_1[\mathbf{y}_h] \leq \lambda_2[\mathbf{y}_h]$ of $\mathbf{I}[\mathbf{y}_h]$ over \mathcal{T}_h satisfy*

$$(76) \quad 0 < c_1 \leq \lambda_1[\mathbf{y}_h] \leq \lambda_2[\mathbf{y}_h] \leq c_2 \quad \forall T \in \mathcal{T}_h,$$

with c_1, c_2 independent of h and T . Then for τ small enough, there exists a constant $c > 0$ independent of h such that

$$(77) \quad \delta^2 L_h^n[\mathbf{y}_h](\mathbf{v}_h, \mathbf{v}_h) \geq c \|\mathbf{v}_h\|_{H^1(\Omega)}^2 \quad \forall \mathbf{v}_h \in \mathbb{V}_h.$$

We next state a Lipschitz property of $\delta^2 L_h^n$ but postpone its proof to Appendix A.

Theorem 4 (Lipschitz property). *Let $\mathbf{y}_h, \tilde{\mathbf{y}}_h \in \mathbb{V}_h$ be given and both satisfy (76). Then, there exists a constant M independent of h such that*

$$(78) \quad |\delta^2 L_h^n[\mathbf{y}_h] - \delta^2 L_h^n[\tilde{\mathbf{y}}_h]|(\mathbf{v}_h, \mathbf{w}_h) \leq \frac{M}{h} \|\mathbf{y}_h - \tilde{\mathbf{y}}_h\|_{H^1(\Omega)} \|\mathbf{v}_h\|_{H^1(\Omega)} \|\mathbf{w}_h\|_{H^1(\Omega)},$$

for any $\mathbf{v}_h, \mathbf{w}_h \in \mathbb{V}_h$.

With Theorems 3 (ellipticity) and 4 (Lipschitz property) at hand, we state an error estimate for each Newton sub-iteration (75) and refer to Appendix A for its proof.

Corollary 3 (quadratic estimate). *If $\mathbf{y}_h^{n,k}$ satisfy (76) for any $n \geq 0$ and $k \geq 0$, then (75) is well-posed and $\delta \mathbf{y}_h^{n,k}$ is the unique solution. Moreover, if $\mathbf{y}_h^{n,k+1} := \mathbf{y}_h^{n,k} + \delta \mathbf{y}_h^{n,k}$, then*

$$(79) \quad \|\mathbf{y}_h^{n,k+1} - \mathbf{y}_h^{n,*}\|_{H^1(\Omega)} \leq \frac{M}{2ch} \|\mathbf{y}_h^{n,k} - \mathbf{y}_h^{n,*}\|_{H^1(\Omega)}^2,$$

where c, M are the constants appearing in (77) and (78) and $\mathbf{y}_h^{n,*}$ is a local minimizer of L_h^n .

Together with a further condition on the initialization $\mathbf{y}_h^{n,0}$, the estimate (79) guarantees the convergence of Newton sub-iterations.

Remark 2 (quadratic convergence). If $\mathbf{y}_h^{n,0}$ satisfies

$$(80) \quad \|\mathbf{y}_h^{n,0} - \mathbf{y}_h^{n,*}\|_{H^1(\Omega)} \leq \frac{ch}{M},$$

then for $k \geq 0$ an induction argument combined with (79) yields

$$(81) \quad \|\mathbf{y}_h^{n,k+1} - \mathbf{y}_h^{n,*}\|_{H^1(\Omega)} \leq \frac{1}{2} \|\mathbf{y}_h^{n,k} - \mathbf{y}_h^{n,*}\|_{H^1(\Omega)} < \frac{ch}{M}.$$

This implies that the Newton sub-iterations $\mathbf{y}_h^{n,k}$ remain within an H^1 -ball of radius $\frac{ch}{M}$ centered at $\mathbf{y}_h^{n,*}$ and converge to $\mathbf{y}_h^{n,*}$; in view of (79) this convergence is quadratic. It remains to check whether the initialization condition (80) is realistic. Assume that $E_h[\mathbf{y}_h^0] \leq \alpha$ for a constant $\alpha > 0$ and recall that $\mathbf{y}_h^{n,0} = \mathbf{y}_h^n$ to deduce

$$\frac{1}{2\tau} \|\mathbf{y}_h^{n,*} - \mathbf{y}_h^n\|_{H^1(\Omega)}^2 \leq L_h^n[\mathbf{y}_h^{n,*}] \leq L_h^n[\mathbf{y}_h^n] = E_h[\mathbf{y}_h^n] \leq E_h[\mathbf{y}_h^0] \leq \alpha.$$

Consequently, if $\tau \leq \frac{c^2 h^2}{2M^2 \alpha}$ then (80) is valid. However, quantitative numerical experiments in our accompanying paper [45] reveal that the largest admissible value of τ is independent of h . This is strikingly better than our theoretical prediction.

Remark 3 (assumption (76)). We now argue heuristically that the crucial assumption (76) is realistic in practice for each iterate $\mathbf{y}_h^{n,k}$ and $n, k \geq 0$. Suppose that $\mathbf{I}[\mathbf{y}_h^{n,k}]$ is close to g pointwise in the sense that

$$(82) \quad \|\mathbf{I}[\mathbf{y}_h^{n,k}] - g\|_{L^\infty(\Omega)} \leq \varepsilon,$$

for some $\varepsilon > 0$. We recall that the eigenvalues of g are λ^2, λ^{-1} with $\lambda > 0$ defined in (11). Then the eigenvalues of $\mathbf{I}[\mathbf{y}_h^{n,k}]$, denoted by $\lambda_1[\mathbf{y}_h^{n,k}] \leq \lambda_2[\mathbf{y}_h^{n,k}]$, satisfy

$$c_1 = \min\{\lambda^2, \lambda^{-1}\} - c\varepsilon \leq \lambda_1[\mathbf{y}_h^{n,k}] \leq \lambda_2[\mathbf{y}_h^{n,k}] \leq \max\{\lambda^2, \lambda^{-1}\} + c\varepsilon = c_2,$$

with some constant $c > 0$. This turns out to be (76) for $\mathbf{y}_h^{n,k}$ provided ε is sufficiently small so that the constants $c_1, c_2 > 0$. Computations in Section 5.6 show conclusively that $\|\mathbf{I}[\mathbf{y}_h^n] - g\|_{L^\infty(\Omega)}$ decreases monotonically as n increases when \mathbf{m} is smooth. They also indicate that $\|\mathbf{I}[\mathbf{y}_h^n] - g\|_{L^1(\Omega)}$ decreases monotonically regardless of the regularity of \mathbf{m} . This gives computational support for (82) and all iterates $\mathbf{y}_h^{n,k}$ provided $\mathbf{I}[\mathbf{y}_h^0]$ is close to the target metric g in the max-norm.

We conclude this section by summarizing the proposed strategy in Algorithm 1.

Algorithm 1: (nonlinear gradient flow scheme)

```

Given a pseudo time-step  $\tau > 0$  and target tolerances  $\text{tol}_1$  and  $\text{tol}_2$ ;
Choose initial guess  $\mathbf{y}_h^0 \in \mathbb{V}_h$ ;
while  $\tau^{-1}|E_h[\mathbf{y}_h^{n+1}] - E_h[\mathbf{y}_h^n]| > \text{tol}_1$  do
    Set  $\mathbf{y}_h^{n,0} = \mathbf{y}_h^n$ ,  $k = 0$ ;
    while  $|\delta L_h^n[\mathbf{y}_h^{n,k}](\delta \mathbf{y}_h^{n,k})|^{1/2} > \text{tol}_2$  do
        Solve (75) for  $\delta \mathbf{y}_h^{n,k}$ ;
        Update  $\mathbf{y}_h^{n,k+1} = \mathbf{y}_h^{n,k} + \delta \mathbf{y}_h^{n,k}$ ,  $k = k + 1$ ;
    end
    Update  $\mathbf{y}_h^{n+1} := \mathbf{y}_h^{n,k}$ , where  $k$  is the index of last sub-iterate.
end

```

5. COMPUTING SHAPES: THE EFFECT OF DEFECTS AND CREASES

We have implemented Algorithm 1 using the multiphysics finite element software Netgen/NGSolve [55], and the visualization relies on ParaView [56]. We refer to our accompanying paper [45] for numerical experiments that show quantitative properties of Algorithm 1 and document the convergence of the proposed method. In this section, we focus on the ability of our discrete reduced model (68) to capture quite appealing and practical physical phenomena related to shape formation.

In some experiments we measure the deviation of $\mathbf{I}[\mathbf{y}_h^\infty]$ from the target metric g for the final iterate \mathbf{y}_h^∞ as an indicator of error between an approximate solution and an exact global minimizer to (9). We quantify this deviation via

$$(83) \quad e_h^p[\mathbf{y}_h^\infty] := \|\mathbf{I}(\mathbf{y}_h^\infty) - g\|_{L^p(\Omega)},$$

for $p = 1, \infty$. Since global minimizers to (9) are characterized by the metric constraint (38) of Corollary 2 (immersions of g are minimizers with vanishing energy), a small metric deviation (83) implies that the approximate solution \mathbf{y}_h^N is close to an exact global minimizer.

5.1. Rotationally symmetric director fields and defects. Consider $\Omega \subset \mathbb{R}^2$ be the unit disc. Motivated by [30, 9, 4, 44], we let the blueprinted director field \mathbf{m} be a rotation of (50) by an angle α

$$(84) \quad \mathbf{m}(r, \theta) = (\cos(n(\theta + \alpha)), \sin(n(\theta + \alpha)));$$

recall that n is the defect degree and that \mathbf{m} is discontinuous at the origin. We run Algorithm 1 with several values of α and n and display the output in Fig. 5. To illustrate the effectiveness of Algorithm 1 to capture physical phenomena, we also compare the computed shapes with experimental and expected configurations in [30, 9] and find striking similarities. We use physical and numerical parameters

$$s = 0.1, s_0 = 1; \quad \text{tol}_1 = 10^{-6}, \text{tol}_2 = 10^{-10}, \tau = 0.1, h = 1/32, c_r = 1,$$

let $\mathbf{x} = (x_1, x_2) \in \Omega$, and initialize Algorithm 1 with $\mathbf{y}_h^0 = I_h \mathbf{y}^0$, where

$$(85) \quad \mathbf{y}^0(\mathbf{x}) = (\mathbf{x}, 0.05(1 - |\mathbf{x}|^2))$$

is a small perturbation of a flat disc (i.e. $\mathbf{y}(\Omega) = \Omega$).

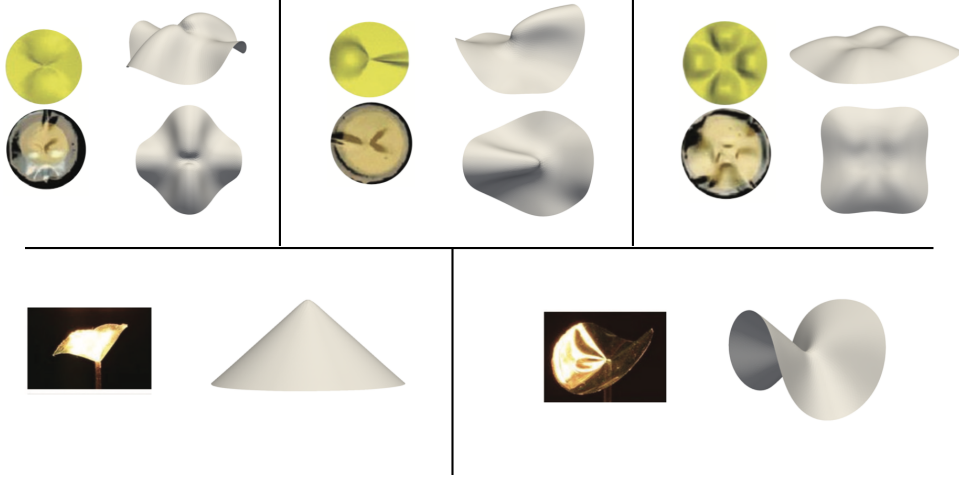


FIGURE 5. *Director fields with point defects of degree n .* First row displays $n = 2, 3/2, -1$ and $\alpha = 0$ (from left to right). Each panel shows experimental and expected configurations from [4] as well as two views of the computed solution. Second row depicts experimental pictures from [57] and our simulations of the cone structure $n = 1, \alpha = \frac{\pi}{2}$ (left) and anti-cone structure $n = 1, \alpha = 0$ (right). The numerical model reproduces experimental observations well.

5.2. Compatible nonisometric origami. Origami are ancient structures made of folding thin sheets. They have recently attracted growing interest in the area of materials science for its practical value in the design of medical devices, deployable space structures and robotics [6]. In this section we explore whether our discrete model (68) with regularization is able to capture such structures.

Motivated by [33, 23, 32], we embark on a computational study of nonisometric origami formed by LCNs. Unlike isometric origami shapes, that arise from pure

folding and bending mechanisms, nonisometric origami result from satisfying the metric constraint (38), i.e. $I[\mathbf{y}] = g$, or equivalently minimizing the stretching energy E_{str} of (9); nonisometric origami thus exhibit stretching and shearing. In each origami experiment below, we split the domain Ω into several subdomains by “folding lines” or “creases” γ_i for $i = 1, \dots, N_\gamma$, and denote the set of them by Γ . We consider fitted meshes to Γ , i.e., $\Gamma \subset \bigcup_{e \in \mathcal{E}_h} e$; see [45] for nonfitted meshes.

Compatibility: We assume the blueprinted director field \mathbf{m} to be constant in each subdomain. We say the set-up of nonisometric origami is *compatible* if

- \mathbf{m} satisfies the compatibility condition proposed in [23, formula (6.3)], namely

$$|\mathbf{m}_{\gamma_i^+} \cdot \mathbf{t}_{\gamma_i}| = |\mathbf{m}_{\gamma_i^-} \cdot \mathbf{t}_{\gamma_i}|,$$

for any $i = 1, \dots, N_\gamma$, where \mathbf{t}_{γ_i} represents a unit tangent vector to γ_i and $\mathbf{m}_{\gamma_i^\pm}$ denote \mathbf{m} restricted to the two subdomains that share γ_i ;

- The actuation parameters s, s_0 , and thus the parameter λ defined in (11), are continuous across γ_i for $i = 1, \dots, N_\gamma$.

The compatibility condition means that the tangential component of the line field $\mathbf{m} \otimes \mathbf{m}$ and parameter λ are continuous across γ_i . Therefore, since any equilibrium configuration satisfies the metric constraint (38) with metric g defined in (36), such configuration sustains *compatible* stretching on both sides of a folding line γ_i .

Moreover, we exploit the fact that the regularization parameter c_r may depend on the edge e to incorporate the creases Γ in the discrete energy E_h in (66). We thus take regularization parameter $c_r = 0$ along the folding lines Γ and $c_r = 100$ in the rest of domain, i.e., we rewrite (67) as

$$(86) \quad R_h[\mathbf{y}_h] = c_r h \sum_{e \in \mathcal{E}_h \setminus \Gamma} \int_e [\nabla \mathbf{y}_h]^2.$$

In fact, the zero regularization (no jumps of gradient) models a weakened (or damaged) material on creases [53], and mathematically this allows for the formation of kinks. On the other hand, the large regularization in the subdomains serves as a mechanism to force small bending energy on minimizers of the discrete stretching energy E_h . Consequently, equilibrium configurations prefer flat surfaces and folds to meet the target metric (38).

5.2.1. *Folding table.* The set-up of blueprinted director field \mathbf{m} , creases Γ and subdomains of $\Omega = [0, 1] \times [0, 2]$ are displayed in Fig.6 (left). We choose parameters

$$s = 0.1, \quad s_0 = 1; \quad h = 1/64, \quad \tau = 0.5, \quad \text{tol}_1 = 10^{-6}, \quad \text{tol}_2 = 10^{-10}.$$

Case 1. We use the initialization $\mathbf{y}_h^0 = I_h \mathbf{y}^0$ with

$$(87) \quad \mathbf{y}^0(x_1, x_2) = (x_1, x_2, 0.8x_1(1-x_1)x_2(2-x_2)).$$

Case 2. We use the initialization $\mathbf{y}_h^0 = I_h \mathbf{y}^0$ with

$$(88) \quad \mathbf{y}^0(x_1, x_2) = (x_1, x_2, 0.8x_1(1-x_1)x_2(1-x_2)).$$

Results for both cases are presented in Fig.6. We get final configurations consistent with the predicted and experimental shapes in [34, Figure 5.2]. The two distinct final states correspond to different initial configurations. However, final energies are $E_h[\mathbf{y}_h^\infty] = 8.27 \times 10^{-6}, 5.97 \times 10^{-6}$ and the metric deviations are $e_h^1[\mathbf{y}_h^\infty] = 4.5 \times 10^{-3}, 3.7 \times 10^{-3}$ for the two cases. Consequently, this provides yet another

example of non-unique minimizers due to the non-convex nature of the discrete model (68); see [45] for further analytical and computational discussions.

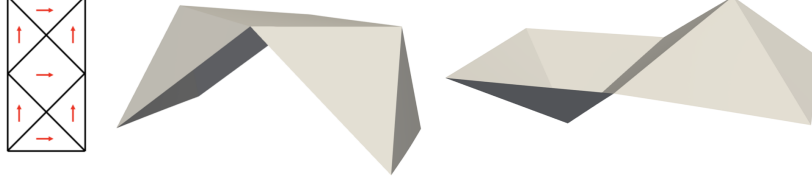


FIGURE 6. *Folding table*: Setting for origami in Subsection 5.2.1 (left). Final configurations for *Case 1* (middle) and *Case 2* (right).

5.2.2. *Folding cube*. We now consider the design in [33] whose folded shape is an origami cube. The set-up is given in Fig.7 (left), where the domain Ω is a rhombus with vertices $(0, 1), (0, 2), (\sqrt{3}, 0), (\sqrt{3}, 1)$. We take a *graded mesh* such that $h = 1/128$ near the creases and $h = 1/32$ everywhere else. We choose the parameters

$$s = -1/3, s_0 = 1; \tau = 0.1, \text{tol}_1 = 10^{-8}, \text{tol}_2 = 10^{-10},$$

and use the initialization $\mathbf{y}_h^0 = I_h \mathbf{y}^0$ with

$$(89) \quad \mathbf{y}^0(x_1, x_2) = \left(x_1, x_2, 0.8x_1(x_1 - \sqrt{3})(x_2 + \frac{\sqrt{3}}{3}x_1 - 1)(x_2 + \frac{\sqrt{3}}{3}x_1 - 2) \right).$$

The evolution of our nonlinear gradient flow is displayed in Fig.7 (right). We reach the desired cube equilibrium configuration with final energy $E_h[\mathbf{y}_h^\infty] = 7.34 \times 10^{-8}$ and metric defect $e_h^1[\mathbf{y}_h^\infty] = 3.6 \times 10^{-4}$.

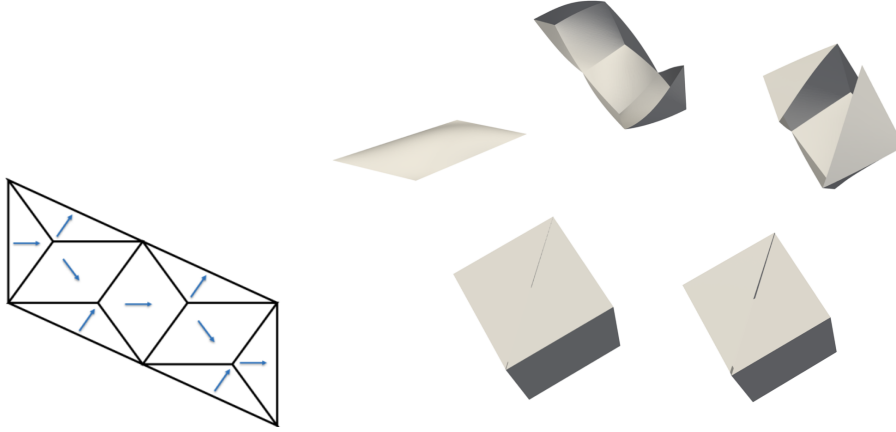


FIGURE 7. *Folding cube*: Rhombus Ω , creases Γ and director field \mathbf{m}_\perp (left). Gradient flow iterates $\mathbf{y}_h^0, \mathbf{y}_h^{110}, \mathbf{y}_h^{310}, \mathbf{y}_h^{1010}$ and final configuration \mathbf{y}_h^{1287} displayed clockwise.

The choice $s = -1/3$ and $s_0 = 1$ is crucial for the shape to form a perfect cube. This can be justified in the spirit of [10] as follows. We expect that rhombi subdomains in Fig. 7 to deform into faces of the cube, which are squares; this is

depicted in Fig. 8. We assume that the diagonals of undeformed rhombi are parallel to $\mathbf{m}_\perp, \mathbf{m}$ and denote their lengths by L_1, L_2 . If $s < s_0$ then $\lambda = \left(\frac{s+1}{s_0+1}\right)^{1/3} < 1$ according to (11), whence the expression (36) of the metric g reveals that the material stretches in the direction \mathbf{m}_\perp and shrinks along \mathbf{m} with ratios $1/\sqrt{\lambda}, \lambda$. If ℓ_1, ℓ_2 stand for the diagonals of the deformed square, then they satisfy $\ell_1 = (1/\sqrt{\lambda})L_1$ and $\ell_2 = \lambda L_2$ as well as $\ell_1 = \ell_2$. Consequently, we see that $\lambda^{-3/2} = L_2/L_1 = \sqrt{3}$ and, choosing $s_0 = 1$, that $s = -1/3$ as asserted.

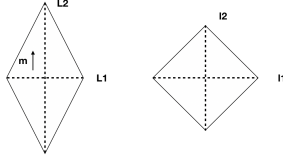


FIGURE 8. *Folding cube*: rhombus with diagonals L_1, L_2 deforms into a square with diagonals $\ell_1 = \ell_2$ to match the target metric and thus minimize the stretching energy.

5.2.3. *Curved creases*. The creases are arcs in this example motivated by [58]. The set-up in Fig. 9 (left) shows that the domain Ω is a square and the creases Γ are curved solid lines. We use a *graded* mesh such that $h = 1/128$ near the arcs and $h = 1/32$ everywhere else. We choose the parameters

$$s = 0.1, \quad s_0 = 1; \quad \tau = 0.5, \quad \text{tol}_1 = 10^{-6}, \quad \text{tol}_2 = 10^{-10},$$

and use the initialization (88). The equilibrium shape is displayed in Fig. 9, which is like a tent. This examples shows the ability of our discrete model (68) to deal with curved creases.

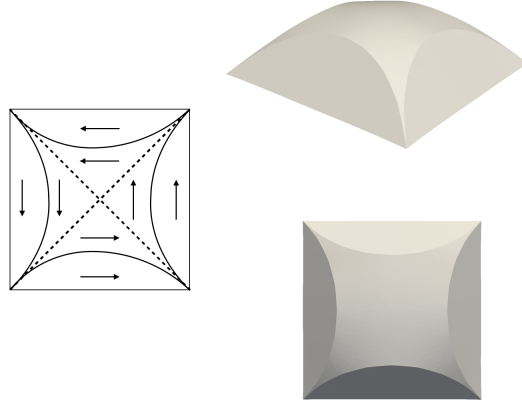


FIGURE 9. *Curved creases*: Square domain Ω , curved creases Γ (solid lines), and director field \mathbf{m} (left). The dashed lines are lines of discontinuity of \mathbf{m} rather than creases. Two views of final tent equilibrium configuration (right).

5.3. Incompatible nonisometric origami. In this section, we allow the physical quantities \mathbf{m}, s, s_0 to *violate* the compatibility condition in Section 5.2, namely to be discontinuous across creases Γ . This entails a discontinuity of g and requires the material to sustain *incompatible* stretching on both sides of the creases. In light of Corollary 2 (immersions of g are minimizers with vanishing energy) and the discussion after it, the existence of an H^1 isometric immersion \mathbf{y} of such a discontinuous g is questionable, and we would hypothesize that there is no deformation $\mathbf{y} \in H^1(\Omega; \mathbb{R}^3)$ such that $\mathbf{I}[\mathbf{y}] = g$ and correspondingly $E_{str, \Gamma}[\mathbf{y}] = 0$, due to the incompatible stretching. Computational evidence given below shows that the discrete energy $E_h[\mathbf{y}_h]$ and metric defect $e_h^1[\mathbf{y}]$ decrease with meshsize to a positive value and the discrete solution \mathbf{y}_h converges, at least weakly, in view of [45, Proposition 2.3 (coercivity)]. We present two simulations and discuss the structure of this limit. To this end, we again consider the modified regularization (86) with $c_r = 0$ along the folding lines and $c_r = 100$ in the rest of the domain.

5.3.1. Lifted square origami. Let $\Omega := [0, 1]^2$ be the unit square and the creases and subdomains be as depicted in Fig. 10 (left). The latter are concentric squares with vertices connected by folding lines. We take $s = s_0 = 1$ in the inner square (ideally no deformation) and $s = 0.1, s_0 = 1$ in the annulus between the two squares so that $\lambda < 1$ in this region. This implies shrinking along the direction of the director field \mathbf{m} , hence parallel to the sides, and stretching in the orthogonal direction \mathbf{m}_\perp .

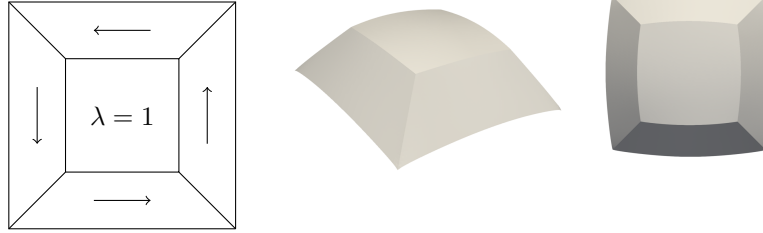


FIGURE 10. *Lifted square origami*: Lines indicate creases and arrows indicate the blueprinted director field \mathbf{m} in regions where $\lambda < 1$ (left). The inner square has $\lambda = 1$ (no internal deformation). Two views of equilibrium configuration show that buckling takes place to accommodate the lack of data compatibility.

We use the initialization (88) and choose the parameters to be

$$h = 1/64, \tau = 0.1, \text{tol}_1 = 10^{-6}, \text{tol}_2 = 10^{-10}.$$

We plot two views of the final configuration on the middle and right of Fig. 10. We see that the inner region has no internally-induced deformation but shrinks and lifts up out of plane to accommodate itself to the change in the outer region.

To explore the asymptotic behavior of \mathbf{y}_h^∞ as $h \rightarrow 0$ we run a series of experiments reported in Fig. 11. We see that the energy $E_h[\mathbf{y}_h^\infty]$ is $\mathcal{O}(10^{-2})$ and decreases but not quadratically; in fact, it seems that it stabilizes to a positive value. Recall that the quadratic scaling $E_h[\mathbf{y}_h] \leq \Lambda h^2$ of (70) in Theorem 1 (convergence of discrete minimizers) leads to strong convergence in $H^1(\Omega; \mathbb{R}^3)$ to a piecewise H^2 -limit \mathbf{y}^*

h	$E_h[\mathbf{y}_h^\infty]$	$e_h^1[\mathbf{y}_h^\infty]$
1/32	0.0277	0.177
1/64	0.0127	0.103
1/128	0.00751	0.0754
1/256	0.00525	0.0626



FIGURE 11. *Lifted square origami*: The table shows a monotone decrease of discrete energy $E_h[\mathbf{y}_h^\infty]$ and metric defect $e_h^1[\mathbf{y}_h^\infty]$ in terms of h , which stabilizes to a positive value. Side views of the deformations for $h = 1/128$ (middle) and $h = 1/64$ (right). The buckling is more pronounced for smaller h .

such that $E_{str,\Gamma}[\mathbf{y}^*] = 0$ and $\mathbf{I}[\mathbf{y}^*] = g$. This reveals that g may not admit an isometric immersion, at least not with the regularity stated in Theorem 1. This in turn contrasts with the compatible origami shapes in Section 5.2 for which the final energies are $\mathcal{O}(10^{-5})$ and $\mathcal{O}(10^{-7})$, making it likely that $E_{str,\Gamma}[\mathbf{y}^*] = 0$.

Fig. 11 also shows that buckling is more pronounced for smaller regularization, which happens for smaller $h = 1/128$. Finally, we view $R_h[\mathbf{y}_h]$ as a numerical mechanism that selects some equilibrium configurations in the limit $h \rightarrow 0$. This process is related to the quasiconvex envelope of E_{str} , which is not known for E_{str} given by (9) and (10) and is hard to find. We refer to [45, Section 2.2.2] for a discussion of quasiconvexity.

5.3.2. Lifted M-origami. We explain now how to exploit the idea in Subsection 5.3.1 as a building block to design lifted configurations of any polygonal shapes. In fact, for any polygonal subdomain $P \subset \Omega := [0, 1]^2$ with $\text{dist}(P, \partial\Omega) > 0$, we can always construct a dilation P' of P so that it is “concentric” with P and $P \subset P'$ with $\text{dist}(P', \partial\Omega) > 0$. Then we further connect corresponding vertices of P and P' with folding lines, and also let all the sides of ∂P and $\partial P'$ be creases. We finally take \mathbf{m} parallel to the sides of ∂P and $\lambda < 1$ in $P' \setminus P$, while $\lambda = 1$ in P and $\Omega \setminus P'$. The discontinuity of λ across creases implies again $E_{str}[\mathbf{y}] > 0$ for all $\mathbf{y} \in H^1(\Omega; \mathbb{R}^3)$.

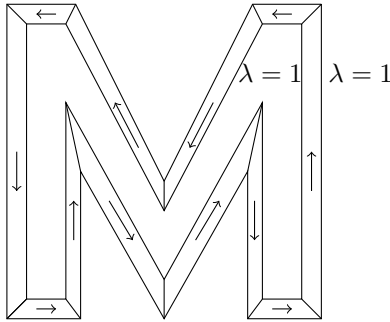


FIGURE 12. *Lifted M-origami*: Lines indicate creases and arrows indicate the blueprinted director field \mathbf{m} in regions where $\lambda < 1$, whereas $\lambda = 1$ within and outside the M.

We apply this procedure to an M-shaped subdomain. The set-up is shown in Fig. 12 and all the parameters are the same as in Subsection 5.3.1. In particular

$s = 0.1$ inside the M-annulus region while $s = 1$ in the rest of domain. We use a graded mesh of size $h = 1/256$ near the creases and otherwise $h = 1/32$.

We display the computed solution in Fig. 13, which is the desired lifted M-shape. We stress that the background and solid M are not completely flat due to the same buckling effect already discussed in Section 5.3.1. However, this effect is not so pronounced because the shrinking layer is thin relative to the rest of the M and background. We emphasize that the current procedure is different from the construction of lifted surfaces in Section 3.1. The latter requires $|\nabla\phi| = \sqrt{\lambda^3 - 1}$ a.e. in Ω , which makes it harder to implement; recall the discussion after (41).

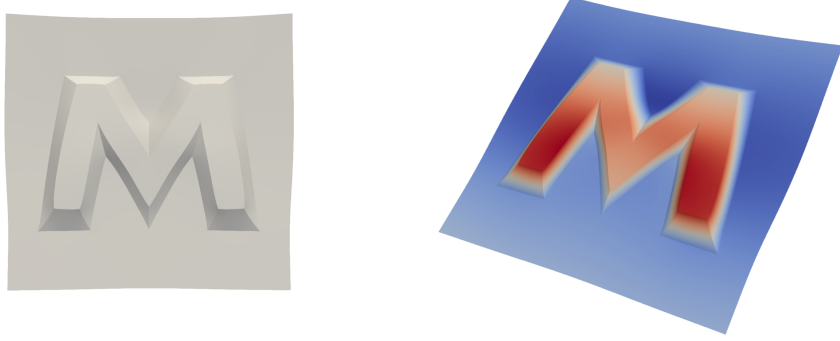


FIGURE 13. *Lifted M-origami*: Two views of final equilibrium configuration. Color on the right picture represents the value of y_3 and shows that the solid M and background are not completely flat.

5.4. Actuation parameters s and s_0 . Parameters s and s_0 encode the effect of environment actuation, such as light and heat, and determine the magnitude of stretches or shrinks in the directions \mathbf{m}_\perp or \mathbf{m} for equilibrium configurations. Therefore, when s is close to s_0 we can only expect a minor deformation; on the other hand, the material deforms significantly if s is far away from s_0 . In this Subsection, we explore the role of s and s_0 by our discrete model (68).

5.4.1. Pyramids with different s . We consider the set-up of Fig.14: the domain is the square $\Omega = [0, 1]^2$, its diagonals are the creases Γ , and the blueprinted director field \mathbf{m} is parallel to the sides of Ω . We choose the parameters

$$s_0 = 1; \quad h = 1/64, \tau = 1, \quad \text{tol}_1 = 10^{-6}, \quad \text{tol}_2 = 10^{-10},$$

regularization constants $c_r = 0$ along the creases and $c_r = 100$ everywhere else, and initialization (88). We take $s = 0.9, 0.5, 0.1, -0.3$ and compare the results.

With arguments similar to those in Subsection 5.2.2 related to Fig. 8, one can easily see that the length of each side of the pyramid base should be $\lambda = (\frac{s+1}{s_0+1})^{\frac{1}{3}}$. In Fig. 15, we compare this theoretical value with computations of such lengths for different values of s , and display the final equilibrium configurations for $s = -0.3, 0.1, 0.5, 0.9$. We observe that the pyramid height decreases to 0 as s increases toward $s_0 = 1$, and thus $\lambda \rightarrow 1$ (no deformation).

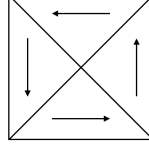


FIGURE 14. Set-up for experiments in Subsection 5.4.1. Square domain Ω with solid diagonals representing the creases and arrows parallel to the sides indicating the piecewise constant blueprinted director field \mathbf{m} .

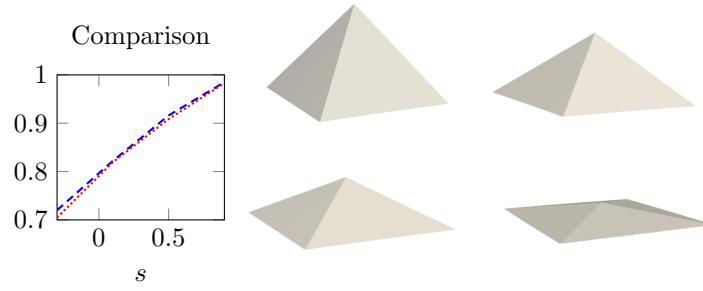


FIGURE 15. *Pyramids with varying actuation parameter s* : Comparison between computed length (blue dashed) and theoretical value $\lambda = (\frac{s+1}{s_0+1})^{\frac{1}{3}}$ (pink dots) of the pyramids base for several values of s (left). Computed pyramid solutions for values $s = -0.3, 0.1, 0.5, 0.9$ approaching $s_0 = 1$ (right).

5.4.2. *Pyramids with space varying s* . All preceding simulations assume s constant in space. We now consider the effect of varying s in space, while keeping all other parameters in Subsection 5.4.1 unchanged. This corresponds, for instance, to the situation that light stimulus is applied non-uniformly to the material. We take

$$(90) \quad s = 1 - 14.4x_1(1 - x_1)x_2(1 - x_2).$$

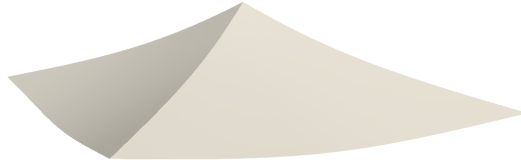


FIGURE 16. *Pyramid with space varying s* : The resulting pyramid for s given in (90) has curved faces, creases and sides.

The computed solution, displayed in Fig.16, consists of a pyramid with curved faces, creases and sides. For the flat pyramids of Fig 15, following [10], we can

predict the opening angle ϕ of the pyramid to satisfy $\sin \phi = \sqrt{\frac{s+1}{s_0+1}}$. The opening angle is formed by two line segments: the vertical line from the vertex of the pyramid to the center of the base and the line segment from the vertex to the midpoint of the side of the base. Since $s_0 = 1$ and s decreases monotonically towards the center of the base from $s = 1$ on the base boundary, we realize that ϕ should decrease as well. This is consistent with our computed solution.

5.4.3. *Four cones.* In this case, we take $\Omega := [-0.5, 0.5]^2$ and parameters

$$s_0 = 1; \quad h = 1/64, \quad \tau = 0.1, \quad \text{tol}_2 = 10^{-10}, \quad \text{tol}_1 = 10^{-6}.$$

We choose the parameters $s = 0.1$ and $c_r = 1$ inside the four circles with radius 0.2 and centers $(\pm 0.25, \pm 0.25)$, and $s = 1$ and $c_r = 100$ everywhere else in the domain. We set the blueprinted director field as in (84), with $n = 1$ and $\alpha = \pi/2$

$$(91) \quad \mathbf{m}(x_1, x_2) = (\cos(\theta_i + \pi/2), \sin(\theta_i + \pi/2))$$

where $\theta_i := \theta_i(x_1, x_2)$ for $i = 1 : 4$ is the angle between the positive x_1 -axis and the line connecting (x_1, x_2) with $(0.25, 0.25)$, $(-0.25, 0.25)$, $(-0.25, -0.25)$, $(0.25, -0.25)$ in each quadrant, respectively. For instance,

$$(92) \quad \theta_1(x_1, x_2) := \begin{cases} \arctan(\frac{x_2-0.25}{x_1-0.25}) & x_1 > 0.25 \\ \arctan(\frac{x_2-0.25}{x_1-0.25}) + \pi & x_1 \leq 0.25. \end{cases}$$

Moreover, we initialize the discrete gradient flow with $\mathbf{y}_h^0 = I_h \mathbf{y}^0$ and

$$(93) \quad \mathbf{y}^0(x_1, x_2) = (x_1, x_2, 0.8(x_1 - 0.5)(x_1 + 0.5)(x_2 - 0.5)(x_2 + 0.5)).$$

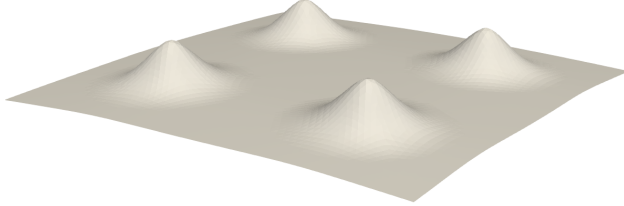


FIGURE 17. *Four cones:* Equilibrium shape showing four rotationally symmetric cones with vertices at $(\pm 0.5, \pm 0.5)$ and curved lateral surfaces. The parameter s and metric g are discontinuous across the boundaries of four circles of radius 0.2 centered at the vertices.

The equilibrium shape is displayed in Fig. 17, and consists of four cones with vertices at the four prescribed points $(\pm 0.25, \pm 0.25)$. Locally around each vertex, the shape is a rotationally symmetric cone as in Subsection 5.1 with $n = 1$ and $\alpha = \pi/2$, but the lateral surface flattens out as it meets the background substrate. This is due to the incompatibility created by the discontinuous parameter s and metric g cross the boundary of the four circles. This configuration is similar to the experimental one in [2].

5.5. Wrinklings and regularizations. We now elaborate on the role of regularization term R_h defined in (67) in the formation of equilibrium configurations.

5.5.1. Degree -1 defect. First, we consider a blueprinted director field \mathbf{m} with a defect of degree $n = -1$ rotated by an angle $\alpha = 0$ as described in (84) of Section 5.1. Fig. 18 compares two simulations with Algorithm 1 and regularization parameter $c_r = 0$ (left) and $c_r = 1$ (right). We observe the formation of wrinklings (or microstructure) at the mesh scale h in final configurations produced when $c_r = 0$ and a smooth shape for $c_r = 1$. We conclude that the regularization term R_h can effectively remove such oscillations.



FIGURE 18. *Degree -1 defect:* Final configurations with $c_r = 0$ (left) and $c_r = 1$ (right) for a director field \mathbf{m} with degree $n = -1$ and $\alpha = 0$ in (84). The regularization term removes oscillations.

5.5.2. Incompatible square origami. We repeat the simulations of Section 5.3.1 with the same parameters except for $c_r = 1$ away from creases Γ (top) and $c_r = 0$ (bottom) of Fig. 19. We learned in Section 5.3.1 that this setting gives rise to *buckling* but, comparing with Fig. 10 when $c_r = 100$ in $\Omega \setminus \Gamma$, we now realize that a smaller regularization parameter leads to a more significant buckling. Moreover, the regularization R_h with $c_r = 1$ removes wrinklings observed for $c_r = 0$.

An illuminating discussion follows about $e_h^1[\mathbf{y}_h^\infty]$ and $E_h[\mathbf{y}_h^\infty]$. We obtain

$$c_r = 100, 1, 0 \Rightarrow e_h^1[\mathbf{y}_h^\infty] \approx 0.1, 0.035, 0.01; E_h[\mathbf{y}_h^\infty] \approx 0.012, 0.0026, 8.9 \times 10^{-4}.$$

Does this mean that the final configuration of Fig. 19 for $c_r = 0$ is closer to a true global minimizer of the stretching energy $E_{str,\Gamma}$ than the others? To elucidate this question, we conduct a mesh analysis for $c_r = 0$ and $c_r = 100$ and report it in Fig. 20. We see that $E_h[\mathbf{y}_h^\infty]$ and $e_h^1[\mathbf{y}_h^\infty]$ converge linearly to 0 for $c_r = 0$, whereas these quantities seem to decrease to a positive value for $c_r = 100$. In contrast, for the compatible pyramid origami of [45, Example 2.2], displayed in Fig. 21, $E_h[\mathbf{y}_h^\infty]$ and $e_h^1[\mathbf{y}_h^\infty]$ can reach the value 10^{-14} by simply reducing the stopping tolerance tol_1 , even for a very coarse meshsize $h = 1/16$. The reason is that an exact solution \mathbf{y}^* for the compatible pyramid origami is *piecewise affine* over \mathcal{T}_h , because \mathcal{T}_h matches the creases, so that $\mathbf{y}^* \in \mathbb{V}_h$. We resort to Corollary 2 (isometric immersions are minimizers with vanishing energy) and Theorem 1 (convergence of discrete minimizers) to infer that there exists a piecewise H^2 isometric immersion for the compatible pyramid origami but not for the incompatible square origami.

We further wonder about the limit of \mathbf{y}_h^∞ as $h \rightarrow 0$ for $c_r = 0$. Although coercivity of the energy $E_h[\mathbf{y}_h^\infty] = E_{str}[\mathbf{y}_h^\infty]$ implies that $\{\mathbf{y}_h^\infty\}_h$ have a weakly

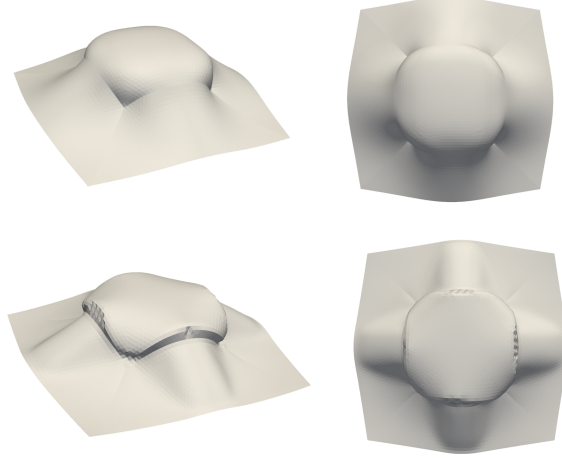


FIGURE 19. *Incompatible square origami*: Two views of the final configurations with regularization parameter $c_r = 1$ (top) and $c_r = 0$ (bottom) away from the creases. Wrinkling occurs for $c_r = 0$.

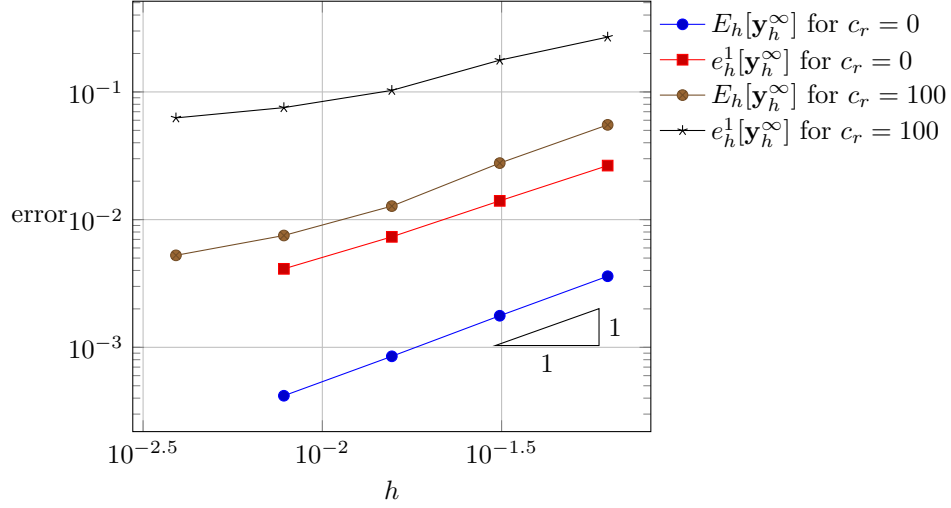


FIGURE 20. *Incompatible square origami*: Plots of $E_h[\mathbf{y}_h^\infty]$ and $e_h^1[\mathbf{y}_h^\infty]$ with several meshsizes h and regularization parameters $c_r = 0, 100$. For $c_r = 0$ we observe that $E_h[\mathbf{y}_h^\infty]$ and $e_h^1[\mathbf{y}_h^\infty]$ are both $\mathcal{O}(h)$, whereas for $c_r = 100$ they stabilize to a positive value as h decreases.

convergent subsequence in $H^1(\Omega; \mathbb{R}^3)$, and we do observe computationally that $E_{str}[\mathbf{y}_h^\infty] \rightarrow 0$, the weak limit \mathbf{y} might not have zero stretching energy due to the lack of quasi-convexity of E_{str} . To illustrate this point we consider again the explicit example of compatible folding pyramids of [45, Example 2.2 and Section 5.1]

with vanishing stretching energy. The sequence $\{\mathbf{y}_i^*\}_{i=1}^\infty$ consists of flat pyramids folding across dyadic concentric creases Γ_i at distance 2^{-i} from each other and matched by the mesh \mathcal{T}_h . The first three discrete solutions $\mathbf{y}_{i,h}^*$ computed by our method are displayed in Fig. 21 and satisfy $\mathbf{y}_{i,h}^* = \mathbf{y}_i^* \in \mathbb{V}_h$ for $i = 1, 2, 3$. The sequence $\{\mathbf{y}_i^*\}_{i=1}^\infty$ converges weakly in $H^1(\Omega; \mathbb{R}^3)$ to $\mathbf{y}^*(\mathbf{x}') = (\lambda \mathbf{x}', 0)^T$ as $i \rightarrow \infty$, but the limit satisfies $E_{str}[\mathbf{y}^*] > 0$. This lack of weak lower semicontinuity of E_{str} in H^1 is related to the lack of quasiconvexity of E_{str} ; we refer to [45, Section 2.2] for details. We can now create a sequence of discrete minimizers $\mathbf{y}_h \in \mathbb{V}_h$ that converge weakly to $\mathbf{y}^*(\mathbf{x}') = (\lambda \mathbf{x}', 0)^T$ as $h \rightarrow 0$: (a) let \mathcal{T}_h be a uniform dyadic partition of Ω made of right triangles with cartesian edges of size $h = 2^{-i}$ for $i \in \mathbb{N}$; (b) let $i(h) = \log_2(1/h)$ and $\mathbf{y}_{i(h)}^*$ be a folding pyramid with creases $\Gamma_{i(h)}$; (c) take $\mathbf{y}_h := \mathbf{y}_{i(h)}^* \in \mathbb{V}_h$ and note that $E_h[\mathbf{y}_h] = 0$. We expect a similar behavior for the incompatible square origami, except that we are not able to characterize the weak limit. Computing the quasiconvex envelope, a key step in this regard, is still open for this problem.

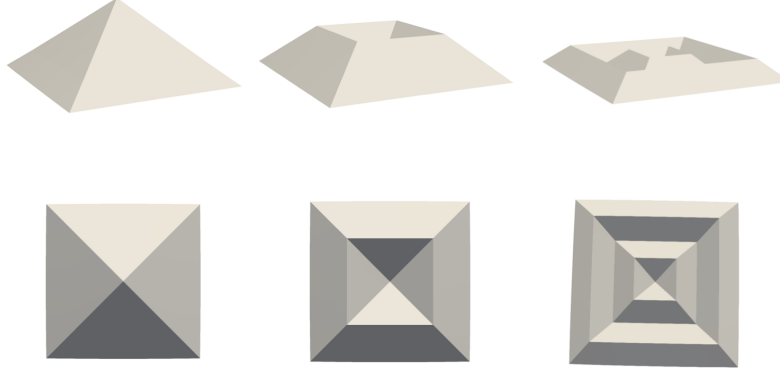


FIGURE 21. *Compatible pyramid origami*: Equilibrium shapes of flat pyramids that fold across dyadic creases as in [45, Section 5.1]. The first and second rows display two views of the same configuration. These explicit deformations converge weakly in H^1 to a non-global minimizer.

We now justify heuristically the shape of \mathbf{y} in Figs. 10 and 19. We observe that any side of the inner square has to shrink by a factor $\lambda < 1$ due to the annulus but remain constant due to the inner square. This incompatible deformation can be realized by developing wrinkles in the inner square with increasing frequency towards the sides so that the length is maintained but accommodated in a shorter interval; a similar mechanism consisting of rapid oscillations towards the domain boundary is studied in [59] for a simplified model. Any approximation of this deformation within the finite element space \mathbb{V}_h introduces the mesh scale h and the effect of regularization $R_h[\mathbf{y}_h]$. The former suppresses infinite wrinkling while the latter prevents the formation of wrinkles at any scale and favors piecewise smooth deformations. Since discrete solutions do not allow infinite oscillations near creases, buckling out of plane is then a natural phenomenon to occur to accommodate

incompatible stretching. Figs. 10 and 19 depict the final configuration and show that the faces and creases are not flat but curved, although all the creases are straight lines in the undeformed configuration.

We may conclude that the regularization (67) serves as a mechanism to select minimizers of stretching energy for *compatible* origami, while a competition between stretching and bending energies determines the final shape for *incompatible* origami.

5.6. Metric errors in the flow. We take $\Omega = [-0.5, 0.5]^2$ and parameters

$$s = 0.1, \quad s_0 = 1; \quad h = 1/64, \quad \tau = 0.48, \quad c_r = 1, \quad \text{tol}_1 = 10^{-6}, \quad \text{tol}_2 = 10^{-10}.$$

Analogously to (87) and (88), we initialize the discrete gradient flow with a perturbation of the flat square $\mathbf{y}_h^0 = I_h \mathbf{y}^0$ where

$$(94) \quad \mathbf{y}^0(x_1, x_2) = (x_1, x_2, 0.8(x_1 - 0.5)(x_1 + 0.5)(x_2 - 0.5)(x_2 + 0.5)).$$

Case 1: Smooth \mathbf{m} . We choose the smooth blueprinted director field

$$(95) \quad \mathbf{m}(x_1, x_2) := (x_1 + 1, x_2 + 1) / \sqrt{(x_1 + 1)^2 + (x_2 + 1)^2}.$$

Case 2: Rough \mathbf{m} . We consider a defect of degree $n = 3/2$ and $\alpha = 0$ in (84).

Fig. 22 contains plots of the metric errors and energies in the discrete gradient flow for both cases. We observe that the energy $E_h[\mathbf{y}_h^n]$ always decays monotonically as expected from Theorem 2 (energy stability). The metric defect $e_h^1[\mathbf{y}_h^n]$ also converges monotonically as n increases in both cases. In contrast, the error $e_h^\infty[\mathbf{y}_h^n]$ decreases monotonically in Case 1 (smooth \mathbf{m}) but not in Case 2 (rough \mathbf{m}). The latter is due to the discontinuity of \mathbf{m} at the origin, hence of the target metric g , but occurs only at the beginning of the flow. The error $e_h^\infty[\mathbf{y}_h^n]$ stabilizes asymptotically but is much larger than $e_h^1[\mathbf{y}_h^n]$. This behavior is consistent with the discontinuity of g but against assumption (82) of Remark 3, in the sense that satisfying (82) for \mathbf{y}_h^0 might not be enough to guarantee (82) for all iterates $\mathbf{y}_h^{n,k}$. Nonetheless, we emphasize again that our Newton sub-iterations always work properly in practice with a simple and straightforward choice of τ rather insensitive to h .

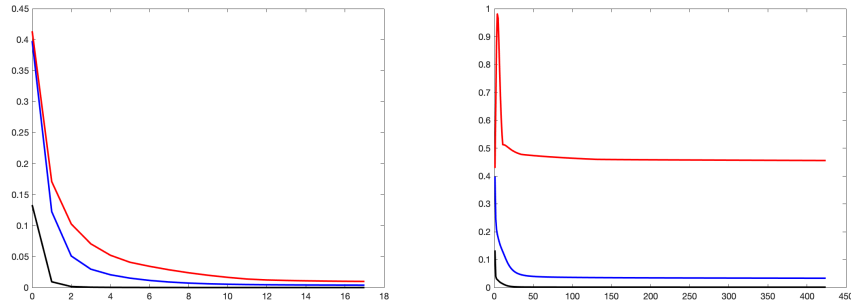


FIGURE 22. Plots of metric errors of $e_h^1[\mathbf{y}_h^n]$ (blue curve), $e_h^\infty[\mathbf{y}_h^n]$ (red curve) and energy $E_h[\mathbf{y}_h^n]$ (black curve) of the gradient flow for $n \geq 0$. Case 1: \mathbf{m} smooth (left) and Case 2: \mathbf{m} rough (right).

6. CONCLUSIONS

This paper deals with a membrane model of nematic liquid crystal polymer networks (LCNs). The two main threads in this paper are asymptotics and computation. Our main contributions are as follows.

- *Modeling:* We use formal asymptotics, in the spirit of [25], to derive a reduced model of LCNs involving the nonconvex stretching energy (9). We prove crucial properties of the model such as the characterization of zero energy states in terms of deformations that satisfy a metric constraint.
- *Asymptotic profiles:* We propose a methodology to find shape profiles corresponding to blueprinted director fields \mathbf{m} with high degree point defects upon composition of defects of degree $n = 1$ and $1/2$. We utilize formal asymptotics to explore shapes for defects of degree $n = 2$ and $n = 3/2$.
- *Discretization:* We propose a finite element method for the stretching energy consisting of continuous piecewise affine functions over a shape regular 2d mesh made of triangles. We augment the discrete stretching energy with a regularization term involving a discrete H^2 -norm. The latter acts as a selection mechanism to prevent oscillations of the solution.
- *Nonlinear solver:* We employ an implicit gradient flow to minimize the discrete energy, and a Newton method to solve each sub-problem. We present a convergence theory for the Newton method based on the coercivity induced by the flow metric and reasonable assumptions on the current iterate. The pseudo time step is not very sensitive to the meshsize and can be taken rather large in practice.
- *Computations:* We present numerous computations highlighting many features of the discrete membrane model. Simulations included shapes coming from LCNs with point defects, nonisometric compatible and incompatible origami, and shapes with spatially varying actuation parameters. We explore computationally the role of regularization and document the decay of the discrete energy and metric defect along the discrete gradient flow.

In the companion paper [45] we prove additional properties of the model, such as the lack of rank-one convexity. We also show in [45] convergence of the finite element solution under a realistic regularity assumption that allows for creases and leads to a quadratic scaling of the discrete energy; see Theorem 1 for details.

ACKNOWLEDGEMENTS

Lucas Bouck was supported by the NSF grant DGE-1840340. Ricardo H. Nochetto and Shuo Yang were partially supported by NSF grant DMS-1908267.

APPENDIX A. NEWTON METHOD: DISCUSSION AND PROOFS

In this appendix we present the lengthy explicit expressions of δE_h and $\delta^2 L_h^n$, as well as proofs of the theorems in Section 4.3.

We first show the expressions of the first variation $\delta E_h[\mathbf{y}_h](\mathbf{v}_h) = \delta E_{str}[\mathbf{y}_h](\mathbf{v}_h) + \delta R_h[\mathbf{y}_h](\mathbf{v}_h)$ at $\mathbf{y}_h \in \mathbb{V}_h$ along the variational direction (or test function) $\mathbf{v}_h \in \mathbb{V}_h$. Since the regularization term is quadratic, its first variation reads

$$\delta R_h[\mathbf{y}_h](\mathbf{v}_h) = 2 \sum_{e \in \mathcal{E}_h} c_r h_e \int_e [\nabla \mathbf{y}_h] : [\nabla \mathbf{v}_h].$$

The first variation of the nonlinear and nonconvex energy E_{str} reads instead

$$\delta E_{str}[\mathbf{y}_h](\mathbf{v}_h) = T_1[\mathbf{y}_h, \mathbf{v}_h] + T_2[\mathbf{y}_h, \mathbf{v}_h] + T_3[\mathbf{y}_h, \mathbf{v}_h] + T_4[\mathbf{y}_h, \mathbf{v}_h],$$

where

$$\begin{aligned} T_1[\mathbf{y}_h, \mathbf{v}_h] &:= - \int_{\Omega} J[\mathbf{y}_h]^{-1} \text{tr} \left(\mathbf{I}[\mathbf{y}_h]^{-1} K[\mathbf{y}_h, \mathbf{v}_h] \right) \\ T_2[\mathbf{y}_h, \mathbf{v}_h] &:= \frac{1}{s+1} \int_{\Omega} \left(2 \nabla \mathbf{y}_h : \nabla \mathbf{v}_h + s_0 \mathbf{m} \cdot K[\mathbf{y}_h, \mathbf{v}_h] \mathbf{m} \right) \\ T_3[\mathbf{y}_h, \mathbf{v}_h] &:= - \frac{s}{s+1} \int_{\Omega} \frac{J[\mathbf{y}_h]}{C_{\mathbf{m}}[\mathbf{y}_h]^2} \mathbf{m} \cdot K[\mathbf{y}_h, \mathbf{v}_h] \mathbf{m} \\ T_4[\mathbf{y}_h, \mathbf{v}_h] &:= \frac{s}{s+1} \int_{\Omega} \frac{J[\mathbf{y}_h]}{C_{\mathbf{m}}[\mathbf{y}_h]} \text{tr} \left(\mathbf{I}[\mathbf{y}_h]^{-1} K[\mathbf{y}_h, \mathbf{v}_h] \right), \end{aligned}$$

and $J[\mathbf{y}_h], C_{\mathbf{m}}[\mathbf{y}_h]$ are defined in (12) and $K[\mathbf{y}_h, \mathbf{v}_h]$ in (14).

We next compute the second order variation of L_h^n at $\mathbf{y}_h \in \mathbb{V}_h$. In fact, we obtain

$$\begin{aligned} (96) \quad \delta^2 L_h^n[\mathbf{y}_h](\mathbf{v}_h, \mathbf{w}_h) &= \frac{1}{\tau} (\mathbf{w}_h, \mathbf{v}_h)_{H^1(\Omega)} \\ &\quad + \delta^2 E_{str}[\mathbf{y}_h](\mathbf{v}_h, \mathbf{w}_h) + \delta^2 R_h[\mathbf{y}_h](\mathbf{v}_h, \mathbf{w}_h), \end{aligned}$$

for arbitrary $\mathbf{v}_h, \mathbf{w}_h \in \mathbb{V}_h$. The last term is actually independent of \mathbf{y}_h and reads

$$(97) \quad \delta^2 R_h[\mathbf{y}_h](\mathbf{v}_h, \mathbf{w}_h) = 2 \sum_{e \in \mathcal{E}_h} \int_e c_r h_e [\nabla \mathbf{v}_h] : [\nabla \mathbf{w}_h].$$

Moreover, the second variation of E_{str} can be written as follows

$$(98) \quad \delta^2 E_{str}[\mathbf{y}_h](\mathbf{v}_h, \mathbf{w}_h) = \sum_{i=1}^4 \delta_{\mathbf{y}_h} T_i[\mathbf{y}_h, \mathbf{v}_h](\mathbf{w}_h),$$

in terms of the first variations of the earlier quantities T_i

$$\begin{aligned} \delta_{\mathbf{y}_h} T_1[\mathbf{y}_h, \mathbf{v}_h](\mathbf{w}_h) &= \int_{\Omega} J[\mathbf{y}_h]^{-1} \text{tr} \left(\mathbf{I}[\mathbf{y}_h]^{-1} K[\mathbf{y}_h, \mathbf{w}_h] \right) \text{tr} \left(\mathbf{I}[\mathbf{y}_h]^{-1} K[\mathbf{y}_h, \mathbf{v}_h] \right) \\ &\quad + \int_{\Omega} J[\mathbf{y}_h]^{-1} \text{tr} \left(\mathbf{I}[\mathbf{y}_h]^{-1} K[\mathbf{y}_h, \mathbf{v}_h] \mathbf{I}[\mathbf{y}_h]^{-1} K[\mathbf{y}_h, \mathbf{w}_h] \right) \\ &\quad - \int_{\Omega} J[\mathbf{y}_h]^{-1} \text{tr} \left(\mathbf{I}[\mathbf{y}_h]^{-1} K[\mathbf{v}_h, \mathbf{w}_h] \right), \\ \delta_{\mathbf{y}_h} T_2[\mathbf{y}_h, \mathbf{v}_h](\mathbf{w}_h) &= \frac{1}{s+1} \int_{\Omega} \left(2 \nabla \mathbf{w}_h : \nabla \mathbf{v}_h + s_0 \mathbf{m} \cdot K[\mathbf{v}_h, \mathbf{w}_h] \mathbf{m} \right), \\ \delta_{\mathbf{y}_h} T_3[\mathbf{y}_h, \mathbf{v}_h](\mathbf{w}_h) &= - \frac{s}{s+1} \int_{\Omega} \frac{J[\mathbf{y}_h]}{C_{\mathbf{m}}[\mathbf{y}_h]^2} \text{tr} \left(\mathbf{I}[\mathbf{y}_h]^{-1} K[\mathbf{y}_h, \mathbf{w}_h] \right) \mathbf{m} \cdot K[\mathbf{y}_h, \mathbf{v}_h] \mathbf{m} \\ &\quad + 2 \frac{s}{s+1} \int_{\Omega} \frac{J[\mathbf{y}_h]}{C_{\mathbf{m}}[\mathbf{y}_h]^3} (\mathbf{m} \cdot K[\mathbf{y}_h, \mathbf{v}_h] \mathbf{m}) (\mathbf{m} \cdot K[\mathbf{y}_h, \mathbf{w}_h] \mathbf{m}) \\ &\quad - \frac{s}{s+1} \int_{\Omega} \frac{J[\mathbf{y}_h]}{C_{\mathbf{m}}[\mathbf{y}_h]^2} \mathbf{m} \cdot K[\mathbf{v}_h, \mathbf{w}_h] \mathbf{m}, \end{aligned}$$

and

$$\begin{aligned} \delta_{\mathbf{y}_h} T_4[\mathbf{y}_h, \mathbf{v}_h](\mathbf{w}_h) &= \frac{s}{s+1} \int_{\Omega} \frac{J[\mathbf{y}_h]}{C_{\mathbf{m}}[\mathbf{y}_h]} \operatorname{tr} \left(\mathbf{I}[\mathbf{y}_h]^{-1} K[\mathbf{y}_h, \mathbf{w}_h] \right) \operatorname{tr} \left(\mathbf{I}[\mathbf{y}_h]^{-1} K[\mathbf{y}_h, \mathbf{v}_h] \right) \\ &\quad - \frac{s}{s+1} \int_{\Omega} \frac{J[\mathbf{y}_h]}{C_{\mathbf{m}}[\mathbf{y}_h]} \operatorname{tr} \left(\mathbf{I}[\mathbf{y}_h]^{-1} K[\mathbf{y}_h, \mathbf{v}_h] \mathbf{I}[\mathbf{y}_h]^{-1} K[\mathbf{y}_h, \mathbf{w}_h] \right) \\ &\quad + \frac{s}{s+1} \int_{\Omega} \frac{J[\mathbf{y}_h]}{C_{\mathbf{m}}[\mathbf{y}_h]} \operatorname{tr} \left(\mathbf{I}[\mathbf{y}_h]^{-1} K[\mathbf{v}_h, \mathbf{w}_h] \right) \\ &\quad - \frac{s}{s+1} \int_{\Omega} \frac{J[\mathbf{y}_h]}{C_{\mathbf{m}}[\mathbf{y}_h]^2} \operatorname{tr} \left(\mathbf{I}[\mathbf{y}_h]^{-1} K[\mathbf{y}_h, \mathbf{v}_h] \right) \mathbf{m} \cdot K[\mathbf{y}_h, \mathbf{w}_h] \mathbf{m}. \end{aligned}$$

We are ready to discuss the proof of ellipticity of $\delta^2 L_h^n$, which requires time-step τ small enough and guarantees the Newton method to be well-posed.

Proof of Theorem 3 (ellipticity). If $\mathbf{w}_h = \mathbf{v}_h$ in (97), this regularization term gives $\delta^2 R_h[\mathbf{y}_h](\mathbf{v}_h, \mathbf{v}_h) = 2R_h[\mathbf{v}_h] > 0$. We only need to estimate the four terms in the expansion of $\delta^2 E_{str}[\mathbf{y}_h](\mathbf{v}_h, \mathbf{v}_h)$ by replacing $\mathbf{w}_h = \mathbf{v}_h$ in (98), and using the flow metric term to control them.

We compute for the piecewise constant quantities $J[\mathbf{y}_h]^{-1}$ and $C_{\mathbf{m}}[\mathbf{y}_h]^{-1}$

$$J[\mathbf{y}_h]^{-1} = \lambda_1^{-1} \lambda_2^{-1} \leq c_1^{-2} \text{ for all } T \in \mathcal{T}_h,$$

and

$$C_{\mathbf{m}}[\mathbf{y}_h]^{-1} \leq \lambda_1^{-1} \leq c_1^{-1} \text{ for all } T \in \mathcal{T}_h.$$

Moreover, one can easily verify that for any SPD 2×2 matrices A, B, C ,

$$\operatorname{tr}(AB) \leq \lambda_{\max}(A)|B|, \quad \operatorname{tr}(ABAC) \leq \lambda_{\max}(A)^2|B||C|.$$

We apply this property to $A = \mathbf{I}[\mathbf{y}_h]^{-1}$, $B = K[\mathbf{y}_h, \mathbf{v}_h]$ and $C = K[\mathbf{y}_h, \mathbf{w}_h]$. Since $\lambda_{\max}(\mathbf{I}[\mathbf{y}_h]^{-1}) = \lambda_1^{-1} < c_1^{-1}$, we obtain

$$|\delta_{\mathbf{y}_h} T_1[\mathbf{y}_h, \mathbf{v}_h](\mathbf{v}_h)| \leq 2c_1^{-4} \|K[\mathbf{y}_h, \mathbf{v}_h]\|_{L^2(\Omega)}^2 + c_1^{-3} \|K[\mathbf{v}_h, \mathbf{v}_h]\|_{L^1(\Omega)}.$$

Moreover, for any 3×2 matrices A, B we have $|A^T B| \leq \sigma_{\max}(A)|B|$, where $\sigma_{\max}(A) := \lambda_{\max}(A^T A)^{\frac{1}{2}}$ is the largest singular value of A . We apply this estimate to $A = \nabla \mathbf{y}_h$ and $B = \nabla \mathbf{v}_h$ to arrive at

$$(99) \quad |K[\mathbf{y}_h, \mathbf{v}_h]|^2 \leq 4 |\nabla \mathbf{y}_h^T \nabla \mathbf{v}_h|^2 \leq 4 \lambda_2 |\nabla \mathbf{v}_h|^2 \leq 4 c_2 |\nabla \mathbf{v}_h|^2,$$

whence $\|K[\mathbf{y}_h, \mathbf{v}_h]\|_{L^2(\Omega)}^2 \leq 4 c_2 \|\nabla \mathbf{v}_h\|_{L^2(\Omega)}^2$. Therefore,

$$|\delta_{\mathbf{y}_h} T_1[\mathbf{y}_h, \mathbf{v}_h](\mathbf{v}_h)| \leq (8c_1^{-4} c_2 + 2c_1^{-3}) \|\nabla \mathbf{v}_h\|_{L^2(\Omega)}^2.$$

Similarly, one can estimate the other terms, and conclude that

$$(100) \quad |\delta_{\mathbf{y}_h} T_j[\mathbf{y}_h, \mathbf{v}_h](\mathbf{v}_h)| \leq C(s, s_0, c_1, c_2, \mathbf{m}) \|\nabla \mathbf{v}_h\|_{L^2(\Omega)}^2 \quad j = 2, 3, 4.$$

Recalling the expression (96) for $\delta^2 L_h^n[\mathbf{y}_h](\mathbf{v}_h, \mathbf{v}_h)$, we realize that choosing τ sufficiently small depending on $s, s_0, c_1, c_2, \mathbf{m}$ yields the desired estimate (77). \square

We next prove the Lipschitz property of $\delta^2 L_h^n$. This is a crucial step towards the convergence of Newton method.

Proof of Theorem 4 (Lipschitz property). To prove (78), we first note that

$$\delta^2 L_h^n[\mathbf{y}_h](\mathbf{v}_h, \mathbf{w}_h) - \delta^2 L_h^n[\tilde{\mathbf{y}}_h](\mathbf{v}_h, \mathbf{w}_h) = \delta^2 E_{str}[\mathbf{y}_h](\mathbf{v}_h, \mathbf{w}_h) - \delta^2 E_{str}[\tilde{\mathbf{y}}_h](\mathbf{v}_h, \mathbf{w}_h),$$

as the flow metric and regularization terms both canceled. Therefore, we only need to check first variations of T_1, T_3, T_4 , because that of T_2 does not depend on \mathbf{y}_h . Since the many ensuing terms can be treated with similar techniques, we illustrate the process with a typical one, namely the second term of $\delta_{\mathbf{y}_h} T_1$. In fact, we denote

$$(101) \quad T_5[\mathbf{y}_h; \mathbf{v}_h, \mathbf{w}_h] := \text{tr}(\mathbf{I}[\mathbf{y}_h]^{-1} K[\mathbf{y}_h, \mathbf{v}_h] \mathbf{I}[\mathbf{y}_h]^{-1} K[\mathbf{y}_h, \mathbf{w}_h]),$$

and observe that $|T_5[\mathbf{y}_h; \mathbf{v}_h, \mathbf{w}_h]| \leq 4c_1^{-2}c_2 |\nabla \mathbf{v}_h| |\nabla \mathbf{w}_h|$, in view of (99), to estimate the second term of $\delta_{\mathbf{y}_h} T_1[\mathbf{y}_h, \mathbf{v}_h](\mathbf{w}_h)$ as follows:

$$\begin{aligned} & \left| \int_{\Omega} J[\mathbf{y}_h]^{-1} T_5[\mathbf{y}_h; \mathbf{v}_h, \mathbf{w}_h] - J[\tilde{\mathbf{y}}_h]^{-1} T_5[\tilde{\mathbf{y}}_h; \mathbf{v}_h, \mathbf{w}_h] \right| \\ & \leq \int_{\Omega} \left| \frac{J[\tilde{\mathbf{y}}_h] T_5[\mathbf{y}_h, \mathbf{v}_h, \mathbf{w}_h] - J[\mathbf{y}_h] T_5[\tilde{\mathbf{y}}_h, \mathbf{v}_h, \mathbf{w}_h]}{J[\mathbf{y}_h] J[\tilde{\mathbf{y}}_h]} \right| \\ & \leq c_1^{-4} \int_{\Omega} \left| J[\mathbf{y}_h] (T_5[\mathbf{y}_h, \mathbf{v}_h, \mathbf{w}_h] - T_5[\tilde{\mathbf{y}}_h, \mathbf{v}_h, \mathbf{w}_h]) \right| \\ & \quad + c_1^{-4} \int_{\Omega} \left| (J[\tilde{\mathbf{y}}_h] - J[\mathbf{y}_h]) T_5[\mathbf{y}_h, \mathbf{v}_h, \mathbf{w}_h] \right| \\ & \leq c_1^{-4} c_2^2 \int_{\Omega} \left| T_5[\mathbf{y}_h, \mathbf{v}_h, \mathbf{w}_h] - T_5[\tilde{\mathbf{y}}_h, \mathbf{v}_h, \mathbf{w}_h] \right| \\ & \quad + 4c_1^{-6} c_2 \int_{\Omega} \left| J[\tilde{\mathbf{y}}_h] - J[\mathbf{y}_h] \right| |\nabla \mathbf{v}_h| |\nabla \mathbf{w}_h|. \end{aligned}$$

We can easily rewrite

$$(102) \quad \left| T_5[\mathbf{y}_h, \mathbf{v}_h, \mathbf{w}_h] - T_5[\tilde{\mathbf{y}}_h, \mathbf{v}_h, \mathbf{w}_h] \right| \leq \sum_{i=6}^9 T_i[\mathbf{y}_h, \tilde{\mathbf{y}}_h, ; \mathbf{v}_h, \mathbf{w}_h],$$

where

$$\begin{aligned} T_6[\mathbf{y}_h, \tilde{\mathbf{y}}_h, ; \mathbf{v}_h, \mathbf{w}_h] &= \left| \text{tr}((\mathbf{I}[\mathbf{y}_h]^{-1} - \mathbf{I}[\tilde{\mathbf{y}}_h]^{-1}) K[\mathbf{y}_h, \mathbf{v}_h] \mathbf{I}[\mathbf{y}_h]^{-1} l(\mathbf{y}_h, \mathbf{w}_h)) \right|, \\ T_7[\mathbf{y}_h, \tilde{\mathbf{y}}_h, ; \mathbf{v}_h, \mathbf{w}_h] &= \left| \text{tr}(\mathbf{I}[\tilde{\mathbf{y}}_h]^{-1} (K[\mathbf{y}_h, \mathbf{v}_h] - K[\tilde{\mathbf{y}}_h, \mathbf{v}_h]) \mathbf{I}[\mathbf{y}_h]^{-1} K[\mathbf{y}_h, \mathbf{w}_h]) \right|, \\ T_8[\mathbf{y}_h, \tilde{\mathbf{y}}_h, ; \mathbf{v}_h, \mathbf{w}_h] &= \left| \text{tr}(\mathbf{I}[\tilde{\mathbf{y}}_h]^{-1} K[\tilde{\mathbf{y}}_h, \mathbf{v}_h] (\mathbf{I}[\mathbf{y}_h]^{-1} - \mathbf{I}[\tilde{\mathbf{y}}_h]^{-1}) K[\mathbf{y}_h, \mathbf{w}_h]) \right|, \\ T_9[\mathbf{y}_h, \tilde{\mathbf{y}}_h, ; \mathbf{v}_h, \mathbf{w}_h] &= \left| \text{tr}(\mathbf{I}[\tilde{\mathbf{y}}_h]^{-1} K[\tilde{\mathbf{y}}_h, \mathbf{v}_h] \mathbf{I}[\tilde{\mathbf{y}}_h]^{-1} (K[\mathbf{y}_h, \mathbf{w}_h] - K[\tilde{\mathbf{y}}_h, \mathbf{w}_h])) \right|. \end{aligned}$$

Note that for SPD 2×2 matrices A, B, C , there holds

$$|\text{tr}((A^{-1} - B^{-1})C)| = |\text{tr}(A^{-1}(B - A)B^{-1}C)| \leq \lambda_{\max}(A^{-1})\lambda_{\max}(B^{-1})|B - A||C|.$$

Using this property and (99), we obtain

$$\begin{aligned} T_6[\mathbf{y}_h, \tilde{\mathbf{y}}_h, ; \mathbf{v}_h, \mathbf{w}_h] &\leq c_1^{-2} |\mathbf{I}[\mathbf{y}_h] - \mathbf{I}[\tilde{\mathbf{y}}_h]| |K[\mathbf{y}_h, \mathbf{v}_h] \mathbf{I}[\mathbf{y}_h]^{-1} K[\mathbf{y}_h, \mathbf{w}_h]| \\ &\leq 4c_1^{-3} c_2 |\mathbf{I}[\mathbf{y}_h] - \mathbf{I}[\tilde{\mathbf{y}}_h]| |\nabla \mathbf{v}_h| |\nabla \mathbf{w}_h| \\ &\leq 4c_1^{-3} c_2^2 |\nabla \mathbf{y}_h - \nabla \tilde{\mathbf{y}}_h| |\nabla \mathbf{v}_h| |\nabla \mathbf{w}_h|, \end{aligned}$$

and a similar estimate for $T_8[\mathbf{y}_h, \tilde{\mathbf{y}}_h, ; \mathbf{v}_h, \mathbf{w}_h]$. Likewise, we can derive

$$T_7[\mathbf{y}_h, \tilde{\mathbf{y}}_h, ; \mathbf{v}_h, \mathbf{w}_h] \leq 4c_1^{-2} c_2^{1/2} |\nabla \mathbf{y}_h - \nabla \tilde{\mathbf{y}}_h| |\nabla \mathbf{v}_h| |\nabla \mathbf{w}_h|,$$

and a similar estimate for $T_9[\mathbf{y}_h, \tilde{\mathbf{y}}_h, ; \mathbf{v}_h, \mathbf{w}_h]$.

Finally, collecting these estimates and resorting to an inverse inequality yields

$$\begin{aligned} \int_{\Omega} \left| T_5[\mathbf{y}_h, \mathbf{v}_h, \mathbf{w}_h] - T_5[\tilde{\mathbf{y}}_h, \mathbf{v}_h, \mathbf{w}_h] \right| \\ \lesssim h^{-1} \|\nabla \mathbf{y}_h - \nabla \tilde{\mathbf{y}}_h\|_{L^2(\Omega)} \|\nabla \mathbf{v}_h\|_{L^2(\Omega)} \|\nabla \mathbf{w}_h\|_{L^2(\Omega)}, \end{aligned}$$

with a hidden constant depending on c_1, c_2 . Moreover, we can easily estimate

$$|J[\tilde{\mathbf{y}}_h] - J[\mathbf{y}_h]| \lesssim |\nabla \tilde{\mathbf{y}}_h - \nabla \mathbf{y}_h|,$$

with a hidden constant depending on c_1, c_2 . This further implies that

$$\left| \int_{\Omega} \frac{T_5[\mathbf{y}_h, \mathbf{v}_h, \mathbf{w}_h]}{J[\mathbf{y}_h]} - \frac{T_5[\tilde{\mathbf{y}}_h, \mathbf{v}_h, \mathbf{w}_h]}{J[\tilde{\mathbf{y}}_h]} \right| \lesssim h^{-1} \|\mathbf{y}_h - \tilde{\mathbf{y}}_h\|_{H^1(\Omega)} \|\mathbf{v}_h\|_{H^1(\Omega)} \|\mathbf{w}_h\|_{H^1(\Omega)}.$$

We can apply the same procedure to all the other terms in $\delta_{\mathbf{y}_h} T_j$ for $j = 1, 3, 4$ to conclude the proof of (78). \square

Theorems 3 (coercivity) and 4 (Lipschitz property) are instrumental to proof the following quadratic estimate of the Newton sub-iterations.

Proof of Corollary 3 (quadratic estimate). Since (76) is satisfied for any $\mathbf{y}_h^{n,k}$ with fixed $n, k \geq 0$ by assumption, the Newton step (75) is well-posed when τ is small enough due to Theorem 3.

We then rewrite (75) as

$$\delta^2 L_h^n[\mathbf{y}_h^{n,k}](\mathbf{y}_h^{n,k+1} - \mathbf{y}_h^{n,*}, \mathbf{v}_h) = \delta^2 L_h^n[\mathbf{y}_h^{n,k}](\mathbf{y}_h^{n,k} - \mathbf{y}_h^{n,*}, \mathbf{v}_h) - \delta L_h^n[\mathbf{y}_h^{n,k}](\mathbf{v}_h),$$

and also

$$\delta L_h^n[\mathbf{y}_h^{n,k}](\mathbf{v}_h) = \int_0^1 \delta^2 L_h^n[\mathbf{y}_h^{n,*} + s(\mathbf{y}_h^{n,k} - \mathbf{y}_h^{n,*})](\mathbf{y}_h^{n,k} - \mathbf{y}_h^{n,*}, \mathbf{v}_h) ds,$$

as $\delta L_h^n[\mathbf{y}_h^{n,*}](\mathbf{v}_h) = 0$ for all $\mathbf{v}_h \in V_h$. Substituting into the preceding equality gives

$$\begin{aligned} \delta^2 L_h^n[\mathbf{y}_h^{n,k}](\mathbf{y}_h^{n,k+1} - \mathbf{y}_h^{n,*}, \mathbf{v}_h) \\ = \int_0^1 \left(\delta^2 L_h^n[\mathbf{y}_h^{n,k}] - \delta^2 L_h^n[\mathbf{y}_h^{n,*} + s(\mathbf{y}_h^{n,k} - \mathbf{y}_h^{n,*})] \right) (\mathbf{y}_h^{n,k} - \mathbf{y}_h^{n,*}, \mathbf{v}_h) ds. \end{aligned}$$

Taking $\mathbf{v}_h = \mathbf{y}_h^{n,k+1} - \mathbf{y}_h^{n,*}$ and using Theorem 3 to estimate the left-hand side from below and Theorem 4 to bound the right-hand side from above yields

$$c \|\mathbf{y}_h^{n,k+1} - \mathbf{y}_h^{n,*}\|_{H^1(\Omega)}^2 \leq \frac{M}{2h} \|\mathbf{y}_h^{n,k} - \mathbf{y}_h^{n,*}\|_{H^1(\Omega)}^2 \|\mathbf{y}_h^{n,k+1} - \mathbf{y}_h^{n,*}\|_{H^1(\Omega)}.$$

This concludes the proof. \square

REFERENCES

- [1] Hillel Aharoni, Yu Xia, Xinyue Zhang, Randall D Kamien, and Shu Yang. Universal inverse design of surfaces with thin nematic elastomer sheets. *Proceedings of the National Academy of Sciences*, 115(28):7206–7211, 2018.
- [2] Taylor H Ware, Michael E McConney, Jeong Jae Wie, Vincent P Tondiglia, and Timothy J White. Voxelated liquid crystal elastomers. *Science*, 347(6225):982–984, 2015.
- [3] Miguel Camacho-Lopez, Heino Finkelmann, Peter Palfy-Muhoray, and Michael Shelley. Fast liquid-crystal elastomer swims into the dark. *Nature Materials*, 3(5):307–310, 2004.
- [4] Michael E McConney, Angel Martinez, Vincent P Tondiglia, Kyung Min Lee, Derrick Langley, Ivan I Smalyukh, and Timothy J White. Topography from topology: photoinduced surface features generated in liquid crystal polymer networks. *Advanced Materials*, 25(41):5880–5885, 2013.

- [5] Kaushik Bhattacharya and Richard D James. The material is the machine. *Science*, 307(5706):53–54, 2005.
- [6] Yao Zhao, Yinding Chi, Yaoye Hong, Yanbin Li, Shu Yang, and Jie Yin. Twisting for soft intelligent autonomous robot in unstructured environments. *Proceedings of the National Academy of Sciences*, 119(22):e2200265119, 2022.
- [7] Min-Hui Li and Patrick Keller. Artificial muscles based on liquid crystal elastomers. *Philosophical Transactions of the Royal Society A: Mathematical, Physical and Engineering Sciences*, 364(1847):2763–2777, 2006.
- [8] Matthieu Hébert, Rama Kant, and Pierre-Gilles De Gennes. Dynamics and thermodynamics of artificial muscles based on nematic gels. *Journal de Physique I*, 7(7):909–919, 1997.
- [9] Timothy J White and Dirk J Broer. Programmable and adaptive mechanics with liquid crystal polymer networks and elastomers. *Nature Materials*, 14(11):1087–1098, 2015.
- [10] Carl D Modes and Mark Warner. Blueprinting nematic glass: Systematically constructing and combining active points of curvature for emergent morphology. *Physical Review E*, 84(2):021711, 2011.
- [11] Mark Warner. Topographic mechanics and applications of liquid crystalline solids. *Annual Review of Condensed Matter Physics*, 11:125–145, 2020.
- [12] Arda Kotikian, Ryan L Truby, John William Boley, Timothy J White, and Jennifer A Lewis. 3d printing of liquid crystal elastomeric actuators with spatially programed nematic order. *Advanced Materials*, 30(10):1706164, 2018.
- [13] Xiao Kuang, Devin J Roach, Jiangtao Wu, Craig M Hamel, Zhen Ding, Tiejun Wang, Martin L Dunn, and Hang Jerry Qi. Advances in 4d printing: materials and applications. *Advanced Functional Materials*, 29(2):1805290, 2019.
- [14] Joselle M McCracken, Brian R Donovan, and Timothy J White. Materials as machines. *Advanced Materials*, 32(20):1906564, 2020.
- [15] P Bladon, Eugene M Terentjev, and Mark Warner. Deformation-induced orientational transitions in liquid crystals elastomer. *Journal de Physique II*, 4(1):75–91, 1994.
- [16] Mark Warner and Eugene M Terentjev. *Liquid crystal elastomers*, volume 120. Oxford university press, 2007.
- [17] Mark Warner and Eugene M Terentjev. Thermal and photo-actuation in nematic elastomers. In *Macromolecular Symposia*, volume 200, pages 81–92. Wiley Online Library, 2003.
- [18] Antonio DeSimone and Luciano Teresi. Elastic energies for nematic elastomers. *The European Physical Journal E*, 29(2):191–204, 2009.
- [19] Pierluigi Cesana, Paul Plucinsky, and Kaushik Bhattacharya. Effective behavior of nematic elastomer membranes. *Archive for Rational Mechanics and Analysis*, 218(2):863–905, 2015.
- [20] Antonio DeSimone and Georg Dolzmann. Macroscopic response of nematic elastomers via relaxation of a class of so (3)-invariant energies. *Archive for Rational Mechanics and Analysis*, 161(3):181–204, 2002.
- [21] Marco Barchiesi and Antonio DeSimone. Frank energy for nematic elastomers: a nonlinear model. *ESAIM: Control, Optimisation and Calculus of Variations*, 21(2):372–377, 2015.
- [22] Chong Luo and Maria-Carme Calderer. Numerical study of liquid crystal elastomers by a mixed finite element method. *European Journal of Applied Mathematics*, 23(1):121–154, 2012.
- [23] Paul Plucinsky, Marius Lemm, and Kaushik Bhattacharya. Actuation of thin nematic elastomer sheets with controlled heterogeneity. *Archive for Rational Mechanics and Analysis*, 227(1):149–214, 2018.
- [24] Sören Bartels, Max Griehl, Stefan Neukamm, David Padilla-Garza, and Christian Palus. A nonlinear bending theory for nematic ice plates. *arXiv preprint arXiv:2203.04010*, 2022.
- [25] Olivier Ozenda, André M Sonnet, and Epifanio G Virga. A blend of stretching and bending in nematic polymer networks. *Soft Matter*, 16(38):8877–8892, 2020.
- [26] Fehmi Cirak, Quan Long, Kaushik Bhattacharya, and Mark Warner. Computational analysis of liquid crystalline elastomer membranes: Changing gaussian curvature without stretch energy. *International Journal of Solids and Structures*, 51(1):144–153, 2014.
- [27] GC Verwey and Mark Warner. Compositional fluctuations and semisoftness in nematic elastomers. *Macromolecules*, 30(14):4189–4195, 1997.
- [28] Haïm Brezis, Jean-Michel Coron, and Elliott H Lieb. Harmonic maps with defects. *Communications in Mathematical Physics*, 107(4):649–705, 1986.

- [29] Sergio Conti and Georg Dolzmann. An adaptive relaxation algorithm for multiscale problems and application to nematic elastomers. *Journal of the Mechanics and Physics of Solids*, 113:126–143, 2018.
- [30] Carl D Modes, Kaushik Bhattacharya, and Mark Warner. Gaussian curvature from flat elastica sheets. *Proceedings of the Royal Society A: Mathematical, Physical and Engineering Sciences*, 467(2128):1121–1140, 2011.
- [31] Cyrus Mostajeran. Curvature generation in nematic surfaces. *Physical Review E*, 91(6):062405, 2015.
- [32] Paul Plucinsky, Benjamin A Kowalski, Timothy J White, and Kaushik Bhattacharya. Patterning nonisometric origami in nematic elastomer sheets. *Soft Matter*, 14(16):3127–3134, 2018.
- [33] Paul Plucinsky, Marius Lemm, and Kaushik Bhattacharya. Programming complex shapes in thin nematic elastomer and glass sheets. *Physical Review E*, 94(1):010701, 2016.
- [34] Paul P Plucinsky. *The deformations of thin nematic elastomer sheets*. PhD thesis, California Institute of Technology, 2017.
- [35] Mark Warner and Cyrus Mostajeran. Nematic director fields and topographies of solid shells of revolution. *Proceedings of the Royal Society A: Mathematical, Physical and Engineering Sciences*, 474(2210):20170566, 2018.
- [36] Hillel Aharoni, Eran Sharon, and Raz Kupferman. Geometry of thin nematic elastomer sheets. *Physical Review Letters*, 113(25):257801, 2014.
- [37] Cyrus Mostajeran, Mark Warner, Taylor H Ware, and Timothy J White. Encoding gaussian curvature in glassy and elastomeric liquid crystal solids. *Proceedings of the Royal Society A: Mathematical, Physical and Engineering Sciences*, 472(2189):20160112, 2016.
- [38] L Angela Mihai and Alain Goriely. A plate theory for nematic liquid crystalline solids. *Journal of the Mechanics and Physics of Solids*, 144:104101, 2020.
- [39] Virginia Agostiniani and Antonio DeSimone. Rigorous derivation of active plate models for thin sheets of nematic elastomers. *Mathematics and Mechanics of Solids*, 25(10):1804–1830, 2020.
- [40] Sören Bartels, Max Griebel, Jakob Keck, and Stefan Neukamm. Modeling and simulation of nematic ice rods. *arXiv preprint arXiv:2205.15174*, 2022.
- [41] Virginia Agostiniani, Antonio DeSimone, and Konstantinos Koumatos. Shape programming for narrow ribbons of nematic elastomers. *Journal of Elasticity*, 127(1):1–24, 2017.
- [42] Harmeet Singh and Epifanio G Virga. A ribbon model for nematic polymer networks. *Journal of Elasticity*, pages 1–22, 2022.
- [43] Sergio Conti, Antonio DeSimone, and Georg Dolzmann. Soft elastic response of stretched sheets of nematic elastomers: a numerical study. *Journal of the Mechanics and Physics of Solids*, 50(7):1431–1451, 2002.
- [44] Hayoung Chung, Jung-Hoon Yun, Joonmyung Choi, and Maenghyo Cho. Finite-element analysis of the optical-texture-mediated photoresponse in a nematic strip. *Computational Mechanics*, 59(1):147–160, 2017.
- [45] Lucas Bouck, Ricardo H. Nochetto, and Shuo Yang. Convergent fem for a membrane model of liquid crystal polymer networks. *arXiv preprint arXiv:2209.04754*, 2022.
- [46] M. Carme Calderer, Carlos A. Garavito Garzón, and Baisheng Yan. A Landau–de Gennes theory of liquid crystal elastomers. *Discrete and Continuous Dynamical Systems - S*, 8(2):283–302, 2015.
- [47] Qing Han and Jia-Xing Hong. *Isometric embedding of Riemannian manifolds in Euclidean spaces*, volume 13. American Mathematical Soc., 2006.
- [48] Bernardo Cockburn, George E Karniadakis, and Chi-Wang Shu. *Discontinuous Galerkin methods: theory, computation and applications*, volume 11. Springer Science & Business Media, 2012.
- [49] Andrea Bonito, Diane Guignard, Ricardo Nochetto, and Shuo Yang. Numerical analysis of the LDG method for large deformations of prestrained plates. *arXiv preprint arXiv:2106.13877*, 2021.
- [50] Sören Bartels. *Numerical methods for nonlinear partial differential equations*, volume 47. Springer, 2015.
- [51] Sören Bartels, Andrea Bonito, and Ricardo H Nochetto. Bilayer plates: Model reduction, γ -convergent finite element approximation, and discrete gradient flow. *Communications on Pure and Applied Mathematics*, 70(3):547–589, 2017.

- [52] Andrea Bonito, Ricardo H Nochetto, and Dimitrios Ntogkas. DG approach to large bending plate deformations with isometry constraint. *Mathematical Models and Methods in Applied Sciences*, 31(01):133–175, 2021.
- [53] Sören Bartels, Andrea Bonito, and Peter Hornung. Modeling and simulation of thin sheet folding. *Interfaces and Free Boundaries*, 2022.
- [54] Sören Bartels, Andrea Bonito, and Philipp Tscherner. Error estimates for a linear folding model. *arXiv preprint arXiv:2205.05720*, 2022.
- [55] Joachim Schöberl et al. Netgen/ngsolve. *Software hosted at <https://ngsolve.org>*, 2017.
- [56] James Ahrens, Berk Geveci, and Charles Law. ParaView: An end-user tool for large data visualization. In Charles D. Hansen and Chris R. Johnson, editors, *Visualization Handbook*, pages 717–731. Elsevier, 2005.
- [57] Laurens T de Haan, Carlos Sánchez-Somolinos, Cees MW Bastiaansen, Albertus PHJ Schenning, and Dirk J Broer. Engineering of complex order and the macroscopic deformation of liquid crystal polymer networks. *Angewandte Chemie*, 124(50):12637–12640, 2012.
- [58] Martin Kilian, Aron Monszpart, and Niloy J Mitra. String actuated curved folded surfaces. *ACM Transactions on Graphics*, 36(3):1–13, 2017.
- [59] Robert V Kohn and Stefan Müller. Surface energy and microstructure in coherent phase transitions. *Communications on Pure and Applied Mathematics*, 47(4):405–435, 1994.

(Lucas Bouck) DEPARTMENT OF MATHEMATICS, UNIVERSITY OF MARYLAND, COLLEGE PARK, MARYLAND 20742, USA.

Email address: lbouck@umd.edu

(Ricardo H. Nochetto) DEPARTMENT OF MATHEMATICS AND INSTITUTE FOR PHYSICAL SCIENCE AND TECHNOLOGY, UNIVERSITY OF MARYLAND, COLLEGE PARK, MARYLAND 20742, USA.

Email address: rhn@umd.edu

(Shuo Yang) YANQI LAKE BEIJING INSTITUTE OF MATHEMATICAL SCIENCES AND APPLICATIONS, BEIJING 101408, CHINA, AND YAU MATHEMATICAL SCIENCES CENTER, TSINGHUA UNIVERSITY, BEIJING 100084, CHINA.

Email address: shuoyang@bimsa.cn